JGR Oceans

RESEARCH ARTICLE
10.1029/2020JC017073

Key Points:

- Interannual variations in altimeter-derived meridional heat transport (MHT) at 26.5°N show good agreement with mooring-based MHT ($r = 0.78$)
- Geostrophic and Ekman transports dominate MHT changes during different time periods
- MHT is highly correlated with the strength of the meridional overturning circulation in both the North and South Atlantic Ocean

Correspondence to:
S. Dong,
Shenfu.Dong@noaa.gov

Citation:
Dong, S., Goni, G., Domingues, R., Bringas, F., Goes, M., Christophersen, J., & Baringer, M. (2021). Synergy of in situ and satellite ocean observations in determining meridional heat transport in the Atlantic Ocean. *Journal of Geophysical Research: Oceans*, *126*, e2020JC017073. https://doi.org/10.1029/2020JC017073

Received 11 DEC 2020
Accepted 17 MAR 2021

Synergy of In Situ and Satellite Ocean Observations in Determining Meridional Heat Transport in the Atlantic Ocean

Shenfu Dong[1], Gustavo Goni[1], Ricardo Domingues[2,1], Francis Bringas[1], Marlos Goes[2,1], Jonathan Christophersen[3], and Molly Baringer[1]

[1]NOAA/Atlantic Oceanographic and Meteorological Laboratory, Miami, FL, USA, [2]Cooperative Institute for Marine and Atmospheric Studies, University of Miami, Miami, USA, [3]National Research Council, U.S. Naval Research Laboratory, Monterey, CA, USA

Abstract The meridional overturning circulation (MOC) is a major driver in global redistribution of heat, which modulates global climate and weather. Altimeter sea surface height measurements and in situ hydrographic data are combined in this work to derive monthly synthetic temperature and salinity (T/S) profiles along zonal transbasin sections in both the North (26.5°N) and South (20°S, 25°S, 30°S, and 35°S) Atlantic Ocean since 1993, which are then used to estimate the MOC and meridional heat transport (MHT). Consistent with previous studies, the results indicate that the MHT is highly correlated with the MOC at all five latitudes. At 26.5°N the mean MHT from synthetic profiles (1.09 ± 0.21 PW) is slightly lower than that from the RAPID-MOCHA-WBTS array (1.20 ± 0.28 PW), but their interannual variabilities show good agreements. Both the geostrophic and Ekman components contribute significantly to the MHT variability, with the geostrophic component dominating during 1993–2004 and the Ekman component dominating during 2005–2014. In the South Atlantic, the MHT seasonal cycle strengthens southward from 20°S to 34.5°S. On interannual time scale, the MHT at 20°S and 25°S experiences larger variations than that at 30°S and 34.5°S, in part due to the fact that the geostrophic and Ekman components work together to strengthen the MHT changes, while they tend to work against each other at 30°S and 34.5°S. Results shown here suggest that integrating data from different observing platforms provides better means to estimate the MOC and MHT in near real time.

Plain Language Summary The Atlantic meridional overturning circulation (AMOC) is an oceanic conveyor belt that transports large amounts of heat northwards throughout the Atlantic Ocean. Variations in the heat carried by the AMOC have pronounced impacts on regional and global extreme weather (hurricanes, heat waves, monsoons, etc.), climate, and sea level. Because of its importance, several efforts from the international community are underway to monitor the AMOC at a few latitudes based on in situ oceanographic instruments. The majority of these estimates, however, only span over relatively short and recent time periods. This study presents 28-year long (1993–2020) estimates of the AMOC volume and heat transports at multiple latitudes (26.5°N, 20°S, 25°S, 30°S, and 34.5°S) by merging in situ oceanographic and satellite observations. These 28-yearlong records indicate that the dominant mechanism causing changes in the strength of this conveyor belt varies between wind forcing and internal ocean dynamics. Therefore, it is important to monitor both fields to fully capture changes in the AMOC system. The methodology presented here provides a means to estimate the AMOC volume and heat transports in near real time, and can be used to validate ocean models, to detect climate variability, and to investigate their impact on extreme weather events.

1. Introduction

The Meridional Overturning Circulation (MOC) plays a fundamental role in modulating the global and regional climate and weather on time scales from seasonal to multi-decadal through global redistribution of heat, salt, and carbon (e.g., Buckley & Marshall, 2016; Lozier 2012; Rahmstorf et al., 2015). Recent studies have shown that variations in the Atlantic MOC (AMOC) may serve as an important driver of changes in the Atlantic sea surface temperature (Duchez et al., 2016; Zhang, 2008), coastal sea level off North America (Little et al., 2017; Volkov et al., 2019), and the strength of the global monsoon circulation and rainfall

(Lopez et al., 2016). A weakened AMOC has also been physically linked as a likely relevant driver of colder North Atlantic and Arctic, extended sea ice cover, higher sea level, and a northward shift of the Intertropical Convergence Zone (e.g., Lorbacher et al., 2010; Stouffer et al., 2006; Vellinga & Wood, 2002; Zhang & Delworth, 2005). The MOC also plays a central role in sequestering carbon from the atmosphere into the deep ocean, which can have long-term implications for the global climate (e.g., Drijfhout et al., 2012; Kostov et al., 2014; Marshall, Armour, et al., 2014, Marshall, Donohoe, et al., 2014; Meehl et al., 2013). Quantifying how the MOC changes over time and understanding the underlying dynamics are, therefore, crucial to advance our knowledge of the weather and climate systems and how they may change in the future.

Research to date has demonstrated that achieving a complete understanding of the time-mean and temporal variability of the MOC system may require a comprehensive and sustained observational network that spans the entire Atlantic basin (e.g., McCarthy et al., 2020). At present, in situ measurements of the MOC are only available at a few latitudes including trans-basin mooring arrays in the subpolar North Atlantic since 2014, at 26.5°N since 2004, and at 34.5°S since 2009 (see detailed summary in Frajka-Williams et al., 2019). MOC estimates from these arrays have revealed energetic variability on timescales from a few days to interannual (e.g., Kersalé et al., 2020; Lozier et al., 2019; Meinen et al., 2018; Srokosz & Bryden, 2015). However, the majority of these MOC estimates are over relatively short-time periods, and hence not long enough to fully understand the MOC variability and its underlying mechanisms. Furthermore, those in situ measurements are generally sparse spatially, and are often not optimal to derive more complex quantities such as the meridional transport of heat and freshwater.

The international community has made several efforts to estimate the AMOC and meridional heat transport (MHT) from alternate approaches by combining in situ measurements (Argo floats, XBTs, CTDs, moorings, etc.) and satellite observations (sea surface height, sea surface temperature, surface winds; Dong et al., 2015; Hobbs & Willis, 2012; Majumder et al., 2016; Mercier et al., 2015; Willis, 2010). These approaches leverage on the more detailed vertical and/or temporal information from in situ measurements and the more detailed temporal and spatial coverage from satellite measurements. This combination allows to estimate the AMOC and MHT at multiple latitudes from 34.5°S (Dong et al., 2015; Majumder et al., 2016) to 41°N (Hobbs & Willis, 2012; Willis, 2010) and over longer time periods than is possible with in situ data alone. Those multi-latitude estimates can be used to investigate the connectivity of the MOC and MHT across the Atlantic Ocean, and to improve our understanding of the driving mechanism and impacts of the MOC variability.

Because Argo floats do not sample regions where ocean floor is shallower than 2,000 m, they miss much of the northward transport carried by the Gulf Stream before it separates from the coast near Cape Hatteras. Similarly in the South Atlantic, Argo floats cannot fully capture the southward transport by the Brazil Current before it separates from the coast at the Brazil-Malvinas Confluence near 36°S. This limits the method in using Argo data as the main source to determine the AMOC to the north of 40°N (Willis, 2010). At 26.5°N, however, the transport of the Florida Current, the Gulf Stream as it passes through the Straits of Florida, has been monitored nearly continuously using submarine telephone cables since 1982. In this study we extend the methodology described in Dong et al. (2015) to the North Atlantic to estimate the MOC and MHT at 26.5°N by combining the synthetic temperature and salinity profiles from hydrographic and altimeter SSH data with the Florida Current transport. In addition, the extended and updated time series of MOC and MHT in the South Atlantic Ocean at four latitudes will also be presented.

The remainder of the study is organized as follows. The data and methods used in the study are described in Section 2. Section 3 provides the evaluation of the methodology. The main results are presented in Section 4, including the MHT variations on seasonal and interannual time scales, and contributions from the geostrophic and Ekman components, and from the overturning and gyre circulations, with more focus on the North Atlantic at 26.5°N. A discussion and summary are given in Sections 5 and 6, respectively.

2. Data and Methodology

The main data set used in this study is the daily satellite altimetry sea surface height anomaly (SSHA) (Pujol et al., 2016) on a 0.25° × 0.25° grid from January 1993 to the October 2020, which is used to derive synthetic temperature and salinity (T/S) profiles along zonal trans-basin sections. In order to derive near-real time MOC and MHT estimates, we use both the delayed time (January 1993–May 2019) and near-real time (June

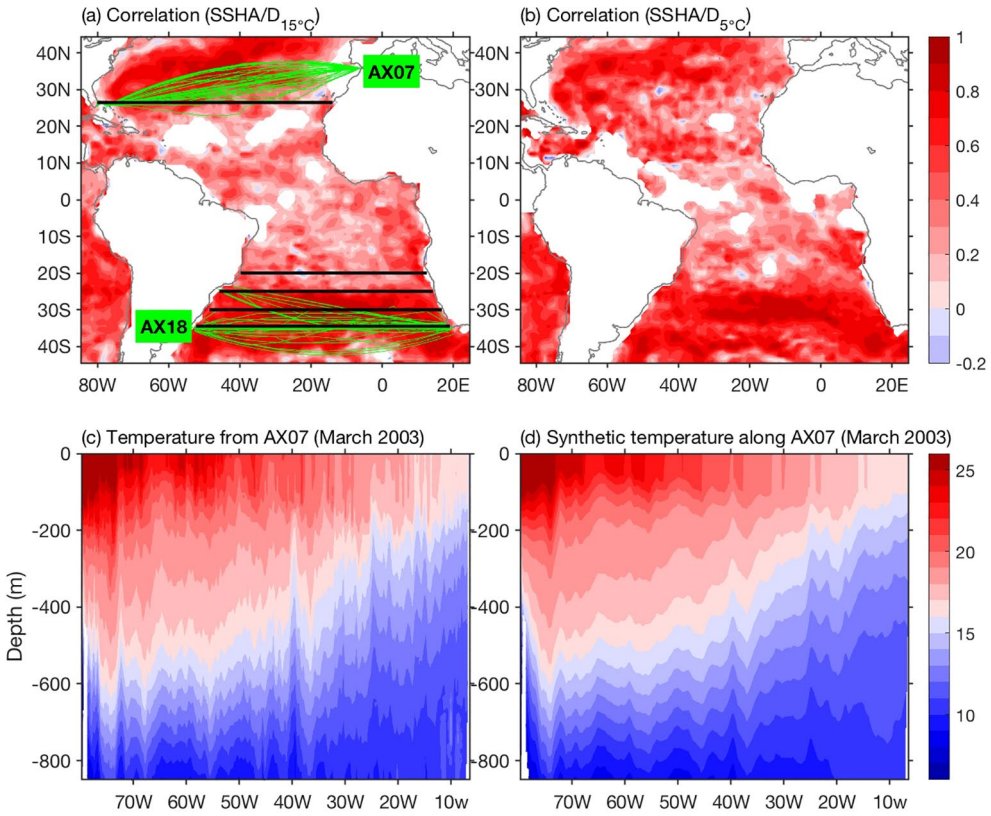

Figure 1. Correlations between SSHA and isothermal depths for (a) 15°C and (b) 5°C. Green lines show the locations of the AX07 transect in the North Atlantic and the AX18 transect in the South Atlantic. (c) An example of the temperature section from XBT AX07 transect in March 2003. (d) The synthetic temperature section along AX07 in March 2003.

2019–October 2020) SSHA. The T/S profiles from the Global Temperature and Salinity Profile Program (GTSPP) (Sun et al., 2010) are used for building statistical relationships between SSHA and depth of isotherms, as described in Goni et al. (1996, 2009). Monthly averages of surface wind stress from the ECMWF Reanalysis 5th Generation (ERA5) on a 0.25° × 0.25° grid are used to derive the Ekman transport.

Dong et al. (2015) described a methodology in deriving MOC and MHT in the South Atlantic Ocean from a combination of satellite altimeter and in situ observations. Here we extend the results from Dong et al. (2015) until 2020, and also apply the same methodology to the North Atlantic at 26.5°N. A brief review of the methodology is provided here. Analysis of collocated SSHA and historical temperature profiles shows significant correlations between SSHA and the depth of given isotherms (D_T) (e.g., $D_{5°C}$ and $D_{15°C}$, Figure 1). These correlations allow for training linear relationships between D_T and SSHA, $D_T = \alpha + \beta \times \text{SSHA}$ at each 1° × 1° grid location for every 1°C of temperature between 3°C and 28°C. Synthetic temperature profiles in the upper ocean at each altimetry grid location can then be generated by feeding gridded SSHA data into these trained statistical relationships with the depth of isotherms. Salinity profiles were generated using the synthetic temperature profiles and historical T/S relationships. The sea surface temperature (SST) for each synthetic profile was obtained from the NOAA 1/4° daily Optimally Interpolated SST version 2. The resulting T & S profiles were extended down to the ocean floor using the Monthly climatological T/S profiles from the World Ocean Atlas 2018 (WOA18). Time series of T/S along five latitudes, 20°S, 25°S, 30°S, 34.5°S, and 26.5°N were then constructed starting in 1993. These trans-basin T/S sections are used to compute geostrophic transport with the reference velocities at 1,000 m depth from Argo drift data (Katsumata & Yoshinari, 2010; Lebedev et al., 2007). These reference velocities are constant in time due to limited available data. In the shallow regions (bottom depth < 1,000 dbar) where Argo drift data are not available, the reference velocities are set to be zero at ocean bottom. The Ekman transport was computed from the ERA5

monthly mean surface wind stress. The heat transport by the Ekman flow was computed assuming the satellite-derived SST as a good representation for temperature conditions in the Ekman layer. A monthly velocity correction, of approximately 0.05 cm/s, was applied uniformly to each monthly section to set the zero-mass transport across the section. The time series of the MOC from 1993 to 2011 were presented in Dong et al. (2015). Besides extending the time series to the present (October 2020) in this study, four improvements are made in the methodology, producing minor differences (±1.0 Sv for MOC, and ±0.05 for MHT) in the final time series compared to what was obtained in Dong et al. (2015):

(1) The synthetic T/S profiles are extended down to 1,000 m depth instead of 800 m
(2) The salinity profiles in the upper 1,000 m are derived using an updated T/S relationship from Goes et al. (2018)
(3) WOA18 monthly T/S climatology is used instead of WOA13 to extend the profiles down to the ocean floor
(4) Ekman transport is computed using monthly wind stress from ERA5 instead of NCEP/DOE Reanalysis 2

The synthetic T/S profiles across 26.5°N are derived with the same methodology as for the South Atlantic. Since the synthetic temperature profiles are computed from the surface to the depth of the 3°C isotherm, along 26.5°N we are able to construct the synthetic profiles down to 1,500 m depth due to the fact that the North Atlantic Ocean is relatively warmer, and the 3°C isotherm is well below the 1,500 m depth. The procedure in deriving the geostrophic transport differs from the South Atlantic in two aspects: (1) transport across the Florida Straits is adjusted to the monthly averages of the Florida Current transport derived from a submarine cable between Florida and the Bahamas (Baringer & Larsen, 2001; Meinen et al., 2010) by applying a uniform velocity correction across the Straits, and (2) following the MOC calculation for the mooring array at 26.5°N (McCarthy et al., 2015), the geostrophic velocity in the interior region (east of the Abaco Island, ~77.5°W) is calculated using a reference level of 1,200 dbar.

NOAA and international partners maintain two transbasin high-density XBT (eXpendable BathyThermographs) transects in the Atlantic Ocean with the main objective of monitoring the MOC and MHT. The MOC and MHT estimates from these two XBT transects are used here to evaluate this synthetic method. The AX07 transect started in 1995 in the North Atlantic along ~30°N between Miami, Florida and Straits of Gibraltar (Figure 1a). In the South Atlantic the AX18 transect started in 2002 along ~34.5°S between Buenos Aires and Cape Town (Figure 1a). Both transects have been carried out approximately four times per year using cargo ships. Along these transects XBTs are deployed with spatial resolution ranging from 10 km near the boundaries to 50 km in the interior region to measure water temperature profiles from the sea surface to a maximum depth of 850 m.

The MHT estimates from the RAPID-MOCHA-WBTS (hereafter referred as RAPID) mooring array at 26.5°N (Johns et al., 2011) and as a residual of energy budget (Trenberth et al., 2019) are used to compare with the estimates from altimetry. The 12-hourly MHT from RAPID is available from April 2004 to August 2018, which is averaged to monthly for comparison. The monthly MHT derived from the energy budget by Trenberth et al. (2019) is available from 33.5°S to 64.5°N on 1° latitude interval for the period June 2000 to May 2016. In the energy budget, the MHT at each latitude (ϕ) was estimated by integrating the net surface heat flux $\phi(F_s)$ and changes in ocean heat content (dOHC/dt) from that latitude to the North Pole ($\mathrm{MHT}_{\phi} = \int_{\phi}^{90}\left[F_S + \left(\mathrm{dOHC}\,/\,\mathrm{dt}\right)\right]\mathrm{d}\phi$). The net surface heat flux was derived from the atmospheric heat flux divergence and top of the atmosphere radiation. Such estimates are also used for comparison purposes against the MHT derived in this study. We note that the MHT estimates from the energy budget at 33.5°S, the southernmost latitude available, are used to compare with our MHT estimates at 34.5°S.

Throughout the study we breakdown the MHT into different components (geostrophic, Ekman, Florida Current, interior, overturning, and gyre) to assess contributions of different processes to MHT variability at seasonal and interannual time scales. Given the fact that the mass flux from some of the components (geostrophic, Ekman, Florida Current, and interior) are non-zero, the heat transports by those components should not be understood as "true heat transports" but as heat transports to a reference temperature of 0°C, as widely applied in literature (e.g., Hall & Bryden, 1982; Johns et al., 2011).

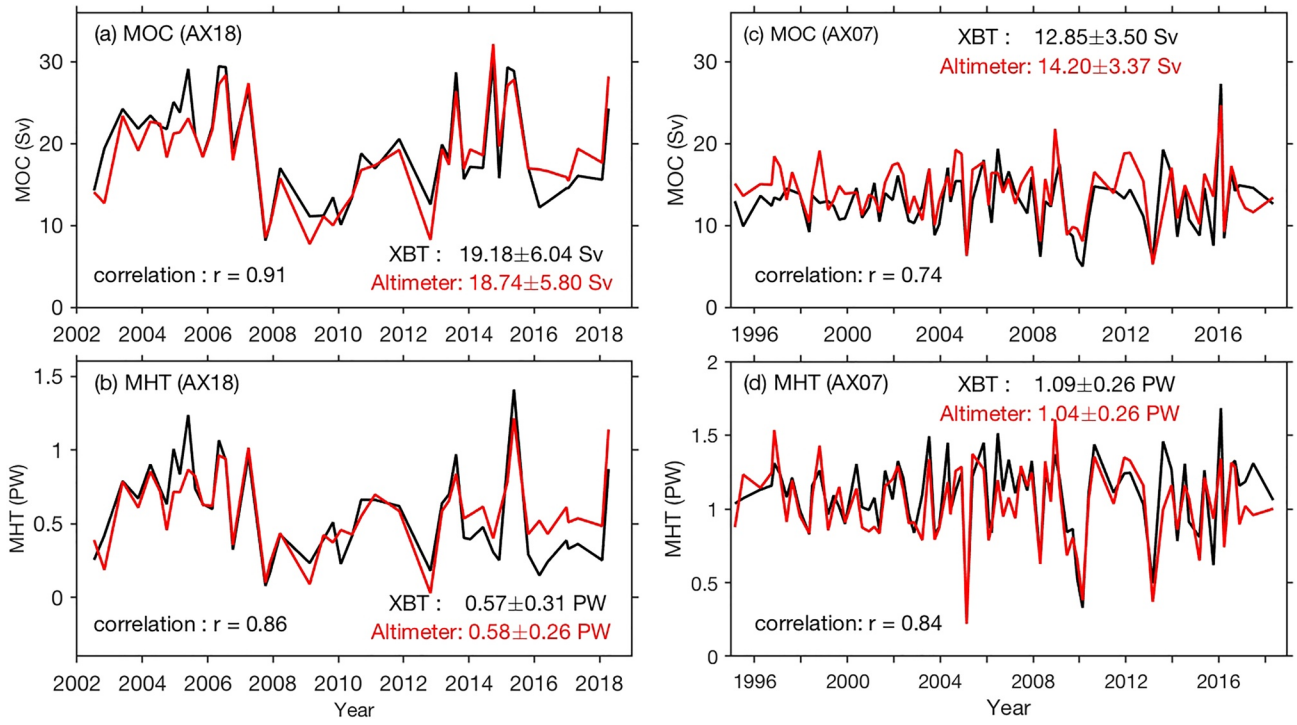

Figure 2. Comparison of the (a) MOC and (b) MHT along XBT transect AX18 in the South Atlantic (~34.5°S) estimated from the XBT measurements (black line) and from the synthetic T/S profiles derived from altimeter SSHA (red line). Panels (c and d) are similar to (a and b) but for the XBT transect AX07 in the North Atlantic (~30°N).

3. Evaluation of the Methodology

In the South Atlantic, the methodology used in deriving MOC and MHT from synthetic T/S profiles was evaluated by comparing with results from the high-density XBT transect AX18 (~34.5°S; Dong et al., 2015). Similarly, we evaluated this methodology in the North Atlantic by comparing results from synthetic T/S sections with results from the concurrent XBT transects along the repeated AX07 transect (Miami to Gibraltar, ~30°N). The synthetic temperature sections are constructed along AX07 with the synthetic temperature profiles matching the location and time of XBT measurements for the 80 in situ realizations of this transect during the period 1995–2018, which includes over 16,220 individual XBT profiles (Figure 1). The synthetic temperature sections are normally smoother than the temperature section observed from XBTs, but they capture well the observed structure both vertically and zonally (Figures 1c and 1d). Although the synthetic temperature profiles reach below 1,500 m, these profiles are cut off at 800 m and extended down to the ocean floor using the monthly climatological T/S profiles from WOA18 for consistency with the XBT measurements. Salinity profiles for each temperature profile (both XBTs and synthetic) are derived using the historical T/S relationship from Goes et al. (2018). MOC and MHT are then computed from T/S sections following the same methodology as described in Section 2 and are shown in Figure 2. For comparison, the updated MOC and MHT time series for XBT AX18 transect and the corresponding synthetic sections during 2002–2018 are also included in Figure 2.

The time-mean and variability (standard deviation, STD) of the altimeter-derived (altimetry plus hydrographic data) MOC and MHT in both the North and South Atlantic are statistically consistent with those calculated using data from the XBT transects (Figure 2). In the North Atlantic, the mean MOC from altimeter (14.20 ± 3.37 Sv) is slight stronger than that from XBTs along AX07 (12.85 ± 3.50 Sv), whereas the mean MHT from altimeter (1.04 ± 0.26 PW) is slight weaker compared to the MHT from AX07 (1.09 ± 0.26 PW). Those differences, however, are not statistically significant. The variations of the MOC and MHT estimates from altimeter also show good comparison with the changes of the MOC and MHT from the AX07 transects, where the correlation coefficients between the XBT- and altimeter-derived MOC and MHT estimates are 0.74 and 0.84, respectively, well above the 95% significance level of 0.28. No statistically significant trends

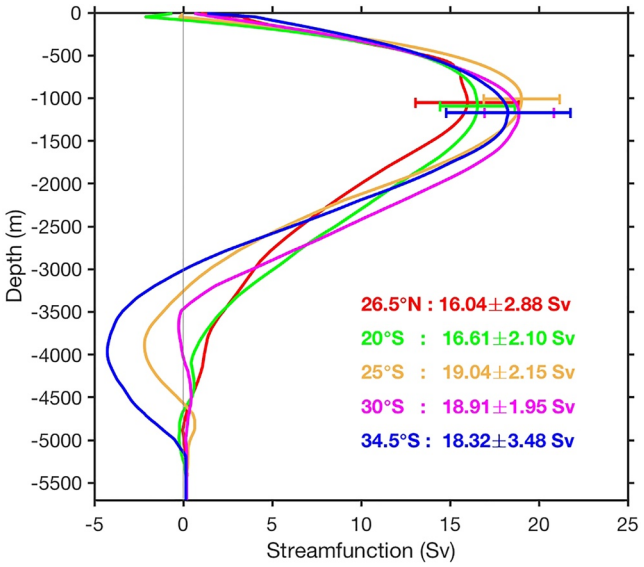

Figure 3. Time-mean MOC streamfunctions at 26.5°N (red), 20°S (green), 25°S (orange), 30°S (magenta), and 34.5°S (blue). The values shown are the mean and variability (standard deviation) of the MOC strength at each latitude.

are found for MOC and MHT during 1995–2018 from both the XBT AX07 transect and the altimeter-derived synthetic sections. These results are consistent with previously reported results for AX18 (Dong et al., 2015), as shown in Figures 2a and 2b. This suggests that the synthetic profiles derived here can successfully capture the changes in the MOC and MHT as observed by XBTs. In addition, the high correlation between the MOC and MHT estimates using XBT and synthetic profiles indicate that the synthetic method described in Section 2 provides a means to estimate the MOC and MHT in near real time, which can be used to monitor the ocean state and to detect climate variability.

4. Results

The time-mean streamfunctions derived from altimetry at all five latitudes during 1993–2020 are shown in Figure 3. At 26.5°N, similar to the results from the RAPID array, the maximum of the streamfunction is found at about 1,000 m depth. Interestingly, we also found the two depth modes of overturning as discussed in McCarthy et al. (2015), a shallower overturning at 750 m and a deeper overturning at 1,070 m depth, which has been attributed to the appearance of the northward flowing Antarctic Intermediate Water. The shallower overturning occurs about 20% of the time during the entire 28-year period. The mean MOC strength from the altimeter is 16.04 Sv with STD of 2.88 Sv, which is slightly weaker than that from the RAPID array (17.66 ± 3.45 Sv), but the difference is not statistically significant. In the South Atlantic, the overturning depths are close to 1,000 m at 20°S and 25°S, and somewhat deeper at 30°S and 34.5°S around 1,200 m. The MOC shows the strongest variability at 34.5°S (±3.48 Sv), nearly double the variability at the other three latitudes from 20°S to 30°S (∼2.0 Sv), due to intensification of the boundary currents at both the eastern and western boundaries and the Agulhas rings shed from the Agulhas Current retroflection.

The time series of the MOC and MHT are shown in Figure 4, and the basic statistics for MHT (record-length mean and temporal standard deviation, seasonal cycle and standard error, and contributions from geostrophic, Ekman, overturning, and gyre components) are listed in Table 1. The MHT shows a positive trend at 34.5°S (0.03 ± 0.01 PW/decade), but no significant trends at the other four latitudes during the full study period (January 1993–October 2020). Significant negative trends in the MOC are observed at 26.5°N (−0.69 ± 0.48 Sv/decade), 20°S (−0.34 ± 0.28 Sv/decade) and 30°S (−0.32 ± 0.21 Sv/decade), while positive trends are observed at 25°S (0.44 ± 0.38 PW/decade) and 34.5°S (0.48 ± 0.36 PW/decade). Further investigation will be conducted to understand the latitudinal variations in trends. The changes in MHT are highly correlated with changes in the MOC at each of these five latitudes, with correlations of 0.89, 0.90, 0.97, 0.90, and 0.93 for 26.5°N, 20°S, 25°S, 30°S, and 34.5°S, respectively. The scatterplot of MOC values against MHT estimates also clearly confirms their close correspondence (Figure 5). Linear regression analysis indicates that at 26.5°N a 1 Sv increase in the MOC would yield a 0.064 ± 0.012 PW increase in the MHT. The geostrophic component of MHT (Q_{geo}) experiences a slightly weaker response to the geostrophic component of the MOC (V_{geo}), with a 0.060 ± 0.008 PW increase in Q_{geo} corresponding to a 1 Sv increase in V_{geo}. The Ekman component of MHT (Q_{ekm}) is much more sensitive to the Ekman volume transport (V_{ekm}) due to the warmer water at the surface, where a 1 Sv increase in V_{ekm} would increase Q_{ekm} by 0.098 ± 0.006 PW. In the South Atlantic, except at 34.5°S, the MHTs between 20°S and 30°S show slightly stronger response to the MOC changes compared to 26.5°N, where a 1 Sv increase in the MOC can result in up to 0.074 ± 0.008 PW increase in the MHT. At all four latitudes the sensitivity of Q_{ekm} to V_{ekm} is weaker than that at 26.5°N (Figure 5), however, it is still considerably stronger than the geostrophic component and the total transport. Given the close correspondence between MOC and MHT, the characteristics of their variability are very similar on both seasonal and interannual time scales. Therefore, our analysis focuses on results for the MHT thereafter.

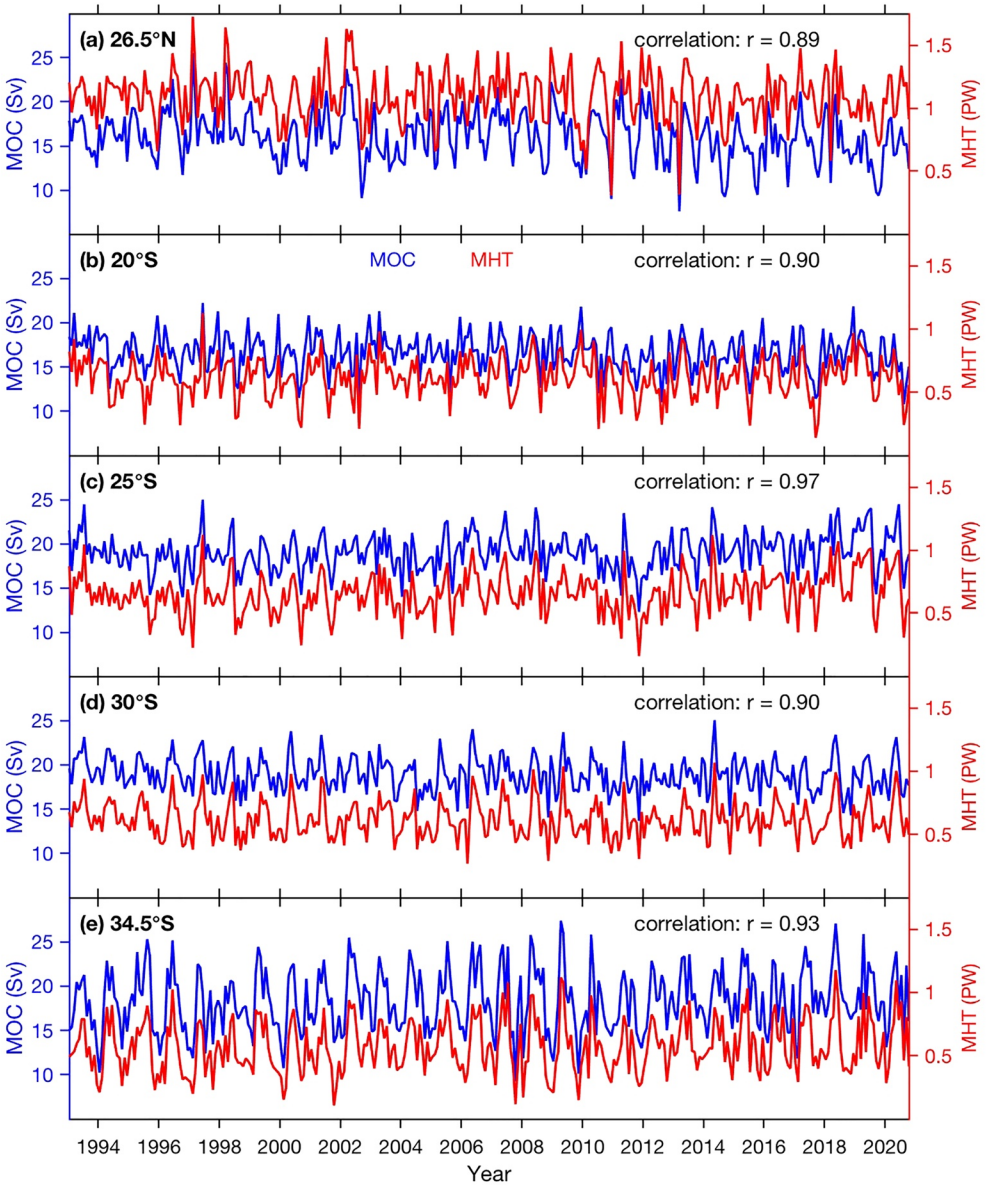

Figure 4. Time series of MOC (blue line, left axis) and MHT (red line, right axis) at (a) 26.5°N, (b) 20°S, (c) 25°S, (d) 30°S, and (e) 34.5°S. Correlation between MOC and MHT at each latitude is included.

4.1. North Atlantic (26.5°N)

4.1.1. Time-Mean

The time-mean MHT at 26.5°N from altimeter during 1993 to 2020 is 1.09 ± 0.21 PW (mean ± STD), which is slightly smaller than the 1.20 ± 0.28 PW from the RAPID mooring array, but larger than the value of 1.06 ± 0.30 PW derived from energy budget by Trenberth et al. (2019). However, all three estimates of mean MHT are statistically comparable. This difference is not due to the different time periods analyzed, as the mean MHT from altimeter during the RAPID period (April 2004–August 2018) is the same as the mean from full time series, 1.09 ± 0.22 PW. The time-mean Ekman component of MHT is 0.35 ± 0.20 PW, very close to the value from the RAPID estimates (0.37 ± 0.22 PW), which is expected since both estimates are based on wind stress from ERA5. Hence, the weaker total MHT from our estimates is mainly associated with a weaker geostrophic heat transport in our estimates (0.75 ± 0.17 PW), which is 0.10 PW lower than that from the RAPID. Further analysis reveals that about 60% of this difference in the Q_{geo} comes from the

Table 1
Time-Mean (±Standard Deviation, STD) and Peak-To-Peak Amplitude of the Annual Cycle (±Standard Error, SE) of the Altimeter-Derived MHT at 26.5°N, 20°S, 25°S, 30°S, and 34.5°S, and the Corresponding Values for Its Contributions From the Geostrophic and Ekman Components, and From Overturning and Gyre Components

MHT (PW)		26.5°N	20°S	25°S	30°S	34.5°S
Mean ± STD	Total	1.09 ± 0.21	0.62 ± 0.16	0.66 ± 0.16	0.62 ± 0.15	0.57 ± 0.21
	Geostrophic	0.75 ± 0.17	1.19 ± 0.09	0.98 ± 0.12	0.66 ± 0.11	0.40 ± 0.16
	Ekman	0.35 ± 0.20	−0.57 ± 0.14	−0.32 ± 0.13	−0.04 ± 0.16	0.17 ± 0.20
	Overturning	0.97 ± 0.20	0.68 ± 0.15	0.82 ± 0.16	0.79 ± 0.14	0.73 ± 0.20
	Gyre	0.12 ± 0.05	−0.06 ± 0.02	−0.17 ± 0.02	−0.17 ± 0.03	−0.16 ± 0.06
Seasonal cycle peak-to-peak amplitude ± SE	Total	0.35 ± 0.05	0.29 ± 0.03	0.30 ± 0.03	0.37 ± 0.02	0.45 ± 0.04
	Geostrophic	0.33 ± 0.03	0.20 ± 0.02	0.21 ± 0.02	0.26 ± 0.02	0.38 ± 0.03
	Ekman	0.28 ± 0.05	0.19 ± 0.03	0.19 ± 0.03	0.38 ± 0.03	0.48 ± 0.03
	Overturning	0.31 ± 0.05	0.28 ± 0.03	0.30 ± 0.03	0.37 ± 0.02	0.46 ± 0.03
	Gyre	0.09 ± 0.01	0.02 ± 0.01	0.03 ± 0.01	0.02 ± 0.01	0.10 ± 0.01

heat transport through the Florida Straits (Q_{FC}). Because the submarine cable only provides the volume transport of the Florida Current, the Q_{FC} in the RAPID result was derived by multiplying a seasonally varying flow weighted temperature derived from the cruise data along 27°N (Johns et al., 2011). This approach likely underestimates interannual changes in the FC temperature, which can be substantial (e.g., Domingues et al., 2018). In this study, we rather directly compute Q_{FC} based through synthetic T/S profiles along 26.5°N that are calculated based on satellite-altimetry and SST observations.

The MHT can be also separated into overturning (Q_{ot}) and gyre (Q_{gyre}) components, defined by

$$Q_{ot} = \int_z \rho c_p \overline{v}(z)\overline{\theta}(z)L(z)dz,$$

$$Q_{gyre} = \int_x \int_z \rho c_p v'(x,z)\theta'(x,z)dxdz,$$

where overbars and primes denote zonal average across the trans-basin section and the deviations from the zonal average. ρ is seawater density, c_p is the specific heat capacity of seawater, v is meridional velocity, θ is potential temperature, and L is the total length of the trans-basin section. Separating the altimeter-derived MHT into overturning and gyre components indicates that about 89% (0.97 ± 0.20 PW) of the MHT is due to the overturning component, with the remaining 11% (0.12 ± 0.05 PW) accounted for by the gyre component, similar to partition between overturning (1.10 ± 0.27 PW, 92%) and gyre (0.10 ± 0.05 PW, 8%) heat transports from the RAPID array during the available period April 2004–August 2018. The Q_{gyre} is mainly contained in the top 700 m of the water column (Figure 6a). The accumulated Q_{gyre} from sea surface to ocean floor reaches its maximum of 0.20 ± 0.06 PW at about 300 m depth, and decreases to 0.11 ± 0.07 PW at 700 m depth, then it slowly increases to 0.12 ± 0.07 PW toward the ocean bottom. Both the vertical accumulated MHT and the overturning component reach their maximum at 1,000 m depth, with values of 1.31 ± 0.23 PW for MHT and 1.19 ± 0.24 PW for Q_{ot}, and they both decrease slowly toward the ocean bottom.

To look into the regional distributions of Q_{gyre}, we examine the zonal distribution of the velocity and temperature deviations from zonal averages. On average, the velocity deviation from the zonal average is positive west of 74°W and negative east of 74°W, whereas the temperature deviation is positive west of 42°W and negative to the east. This results in positive (northward) heat transport from the gyre circulation west of 74°W (0.09 ± 0.06 PW) and east of 42°W (0.09 ± 0.04 PW), and negative (southward) heat transport from the gyre circulation between 74°W and 43°W (−0.06 ± 0.04 PW). This spatial structure of the gyre component is clearly illustrated by the accumulated Q_{gyre} from west to east, shown in Figure 6b. The contribution

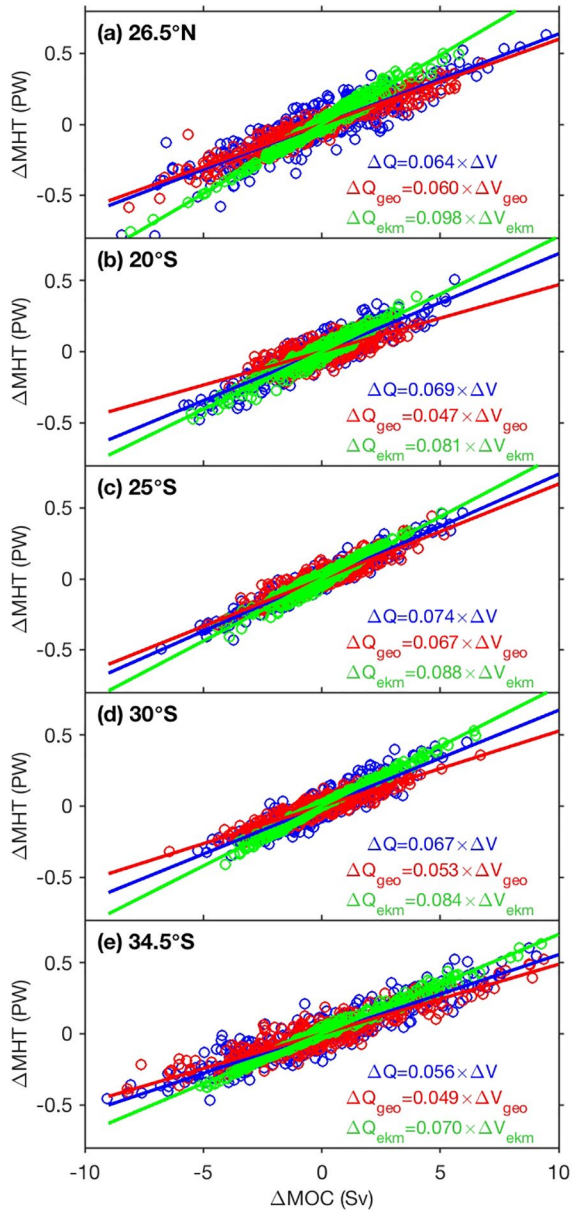

Figure 5. Scatterplots of MHT anomalies against MOC anomalies (blue circles) at (a) 26.5°N, (b) 20°S, (c) 25°S, (d) 30°S, and (e) 34.5°S. The red and green circles are for the geostrophic and Ekman components, respectively.

from the Florida Current is rather small (0.03 ± 0.04 PW) due to negative temperature deviations from zonal averages below 300 m depth.

4.1.2. Seasonal Cycle

The monthly climatological averages of the altimeter-based MHT show the peak-to-peak amplitude of its seasonal signal of 0.35 PW with standard error of 0.05 PW. The maximum in MHT occurs in July and minimum in October (Figure 7). This amplitude is weaker than that from the RAPID array (0.48 ± 0.10 PW), but not statistically different. However, there are large differences in the phase of their seasonal evolution. Although the MHT from the RAPID also peaks around July, RAPID estimates show negative anomalies (i.e., mean subtracted) from January to May and positive anomalies from June to December, whereas our estimates show positive anomalies from April to August and negative anomalies from September to December. The phase of the altimeter-based MHT seasonal variation shows better agreement with that from Trenberth et al. (2019) which has positive anomalies from March to August and negative anomalies from September to February, but the amplitude is about half of their estimate of 0.69 ± 0.07 PW. These differences in terms of seasonality cannot be explained by the different temporal coverage, as the seasonal cycle of the altimeter-based MHT is essentially unchanged when we confine the altimeter results to the same time period as the mooring array. Since the wind stress and Florida Current are in close match, the difference comes from the interior geostrophic heat transport. As discussed in Section 5, this discrepancy in the interior geostrophic transport is linked to the differences in dynamic height products between the RAPID moorings and satellite altimeter at both the eastern and western boundaries. The RAPID moorings do not sample the upper 100 m water column where the seasonal variations are primarily contained, and the T/S profiles were extrapolated to the surface (McCarthy et al., 2015). The extent to which this extrapolation contributes to the discrepancy of the seasonal cycle in the interior transports is still unclear and requires further investigation.

Both geostrophic (Q_{geo}) and Ekman (Q_{ekm}) contributions to MHT experience seasonal variations (Figure 8a), but they are out of phase. The amplitude (peak-to-peak) of the seasonal cycle in Q_{geo} is 0.33 ± 0.03 PW, with positive anomalies from February to July and negative anomalies from August to January. Q_{geo} reaches its maximum in April and minimum in November. The seasonal cycle of Q_{ekm} has an amplitude of 0.28 ± 0.05 PW, it is nearly 180° out of phase with Q_{geo}. Because of the relatively larger anomalies in Q_{geo}, the phase of the seasonal variation of MHT follows primarily the seasonal evolution of Q_{geo}, except for the maximum in July, which is dominated by Q_{ekm}. The seasonal variation accounts for a significant amount (41%) of the total variance in Q_{geo}. For total MHT and Q_{ekm}, the seasonal signal only explains 18% and 19% of their total variance, respectively. Despite the phase difference in the seasonal variations of the MHT from the RAPID array, the altimeter estimates draw the same conclusion as pointed out by Johns et al. (2011) that, unlike results from numerical models which suggested that the seasonal variations in the MHT at 26.5°N are dominated by the Ekman heat transport (Boning et al., 2001; Jayne & Marotzke, 2001), both the geostrophic and Ekman components contribute significantly to the seasonal evolution of the MHT, with the Q_{geo} playing a slightly larger role.

Examination of the overturning and gyre contributions to the MHT indicates that the seasonal variations in the overturning heat transport largely control the amplitude and phase of the total MHT seasonal evolution, with peak-to-peak amplitude of 0.31 ± 0.05 PW (Figure 8b). The overturning heat transport shows positive

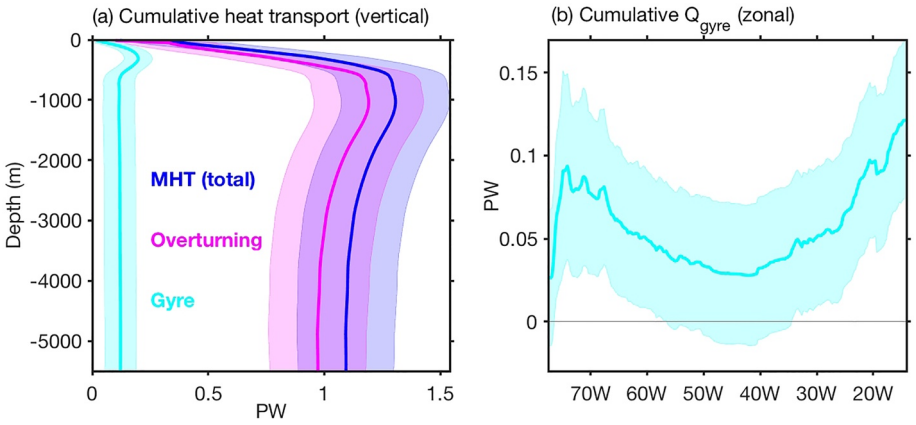

Figure 6. (a) Cumulative meridional heat transport (blue) at 26.5°N and its contributions from the overturning (magenta) and gyre circulation (cyan) from sea surface to the ocean floor. (b) Cumulative heat transport from gyre circulation from west to east. Shading around each curve indicates two standard deviations.

anomalies from January to August and negative anomalies from September to December, which is due to the seasonal changes in the strength of the MOC. The seasonal cycle in the gyre heat transport is weak, peak-to-peak amplitude of 0.09 ± 0.01 PW, with positive anomalies during April to October and negative anomalies from November to March. More than 90% of the seasonal variation in the Q_{gyre} can be explained by the seasonal changes in temperature deviation from the zonal average, which mainly comes from the Florida Straits region. Although the Q_{FC} has minimal contribution to the time-mean Q_{gyre}, it accounts for 78% of the seasonal changes in the Q_{gyre}. The amplitude of the gyre contribution is close to the value of 0.12 ± 0.02 PW from the RAPID array, and their phases are also consistent. However, similar to the total MHT, the amplitude of the overturning contribution is weaker than that from the RAPID array (0.43 ± 0.10 PW), and their phases are different due to difference in the interior geostrophic heat transport.

4.1.3. Interannual Variations

The monthly anomalies of the MHT at 26.5°N from altimeter-derived synthetic T/S sections and RAPID mooring after removing the seasonal signal are shown in Figure 9, which are significantly correlated ($r = 0.82$). Also shown in Figure 9 is the interannual variations after low-pass filtering to remove signals with periods less than a year. Different from seasonal variations, on interannual time scales the altimeter-derived MHT estimates show good agreement with the MHT changes derived from both the RAPID array and the energy budget method (Figure 9), with correlations of 0.78 and 0.65, respectively. The largest difference in MHT between the altimeter-based and the RAPID estimates is seen at the beginning of the RAPID period around 2005–2006, during which the MHT anomalies from RAPID show large positive values, whereas the anomalies derived from satellite altimetry are rather small. As previously suggested by Trenberth et al. (2019), the large positive anomalies in RAPID estimates may be related to mooring issues during the early period. In addition, all three MHT estimates show subtle decreasing trends during the overlapping time period (April 2004–May 2016) of: −0.08 ± 0.09 PW/decade for altimeter-based; −0.18 ± 0.16 PW/decade for RAPID; and −0.07 ± 0.12 PW/decade from energy budget calculations. However, only the trend from RAPID estimates is statistically significant considering a 95% confidence level, while the trends from altimeter and energy budget are not statistically different from zero. The trend in the RAPID estimates is mainly due to the large positive anomalies in 2005–2006.

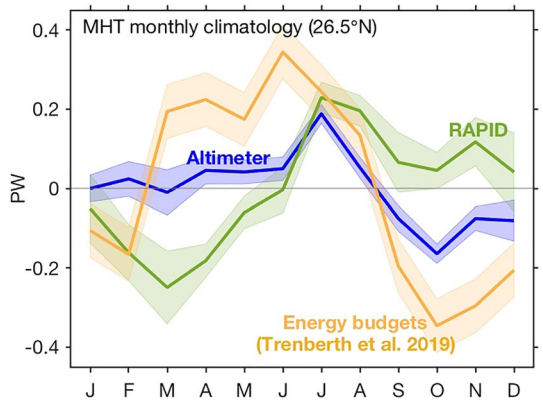

Figure 7. Seasonal variations of the MHT at 26.5°N estimated from altimeter synthetic T/S profiles (blue), the RAPID array (dark green), and the energy budgets (orange). The time-mean values for the MHT have been removed. Shading around each curve indicates two standard errors.

Both the geostrophic and Ekman components of the MHT contribute to its interannual variations (Figure 10a), but they dominate MHT anomalies during different time periods. For example, the Q_{geo} plays a dominant role in MHT variations during 1998–2003, 2014–2015 and 2019, and the

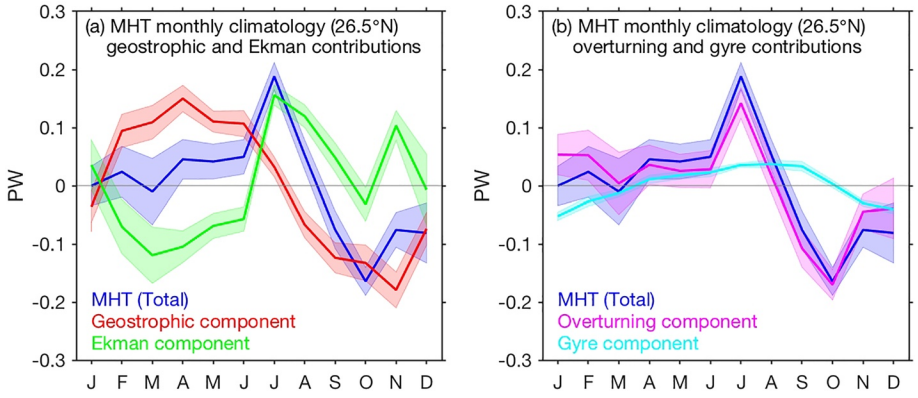

Figure 8. (a) Seasonal variations of the MHT (blue) and contributions from the geostrophic (red) and Ekman (green) components estimated from synthetic T/S profiles at 26.5°N. The time-mean values for the total MHT and each component have been removed. (b) Similar to (a), but for contributions from the overturning (magenta) and gyre (cyan) components. Shading around each curve indicates two standard errors.

Q_{ekm} dominates during 2009–2013. Figure 10b suggests that this changing dominance is induced to some extent by the strength of the Florida Current transport anomalies. As a result, we see a stronger relationship between MHT and Q_{geo} during 1993–2004 with a correlation of 0.75, but their correlation ($r = 0.18$) is lower during the following 10 years between 2005 and 2014. On the contrary, the correlation between MHT and Q_{ekm} is low during 1993–2004 ($r = 0.12$), but quite high during 2005–2014 ($r = 0.75$). This changing relationship suggests the importance of continuously monitoring the MHT in order to fully understand its variability and contributions from different processes over a longer time period. For the entire study period (1993–2020), the MHT shows a significant correlation with its geostrophic contribution ($r = 0.60$) but not with the Ekman contribution ($r = 0.35$) on the 95% significance level (0.37), suggesting that the Q_{geo} plays a somewhat larger role in the interannual variations of the total MHT. Figure 7a also shows that the Q_{geo} and Q_{ekm} are negatively correlated ($r = -0.54$), and they act to damp each other during the majority of the time.

The Q_{geo} shows a marginal decreasing trend of -0.04 ± 0.03 PW/decade during 1993–2020, which is due to the decrease in the volume transport by the geostrophic flow (-0.74 ± 0.58 Sv/decade). Whereas the Q_{ekm} shows an increasing trend (0.02 ± 0.03 PW/decade), but not statistically different from zero. Separating

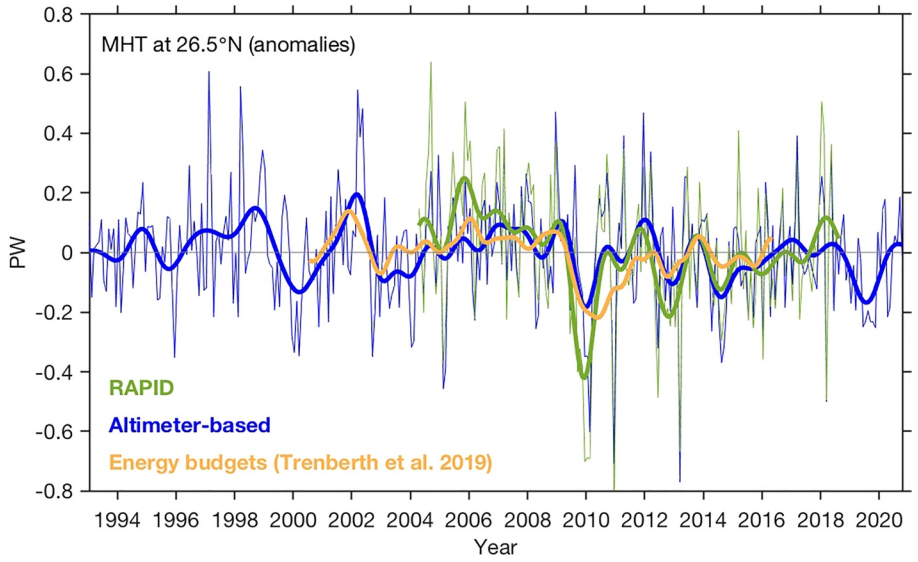

Figure 9. Monthly anomalies of the MHT at 26.5°N from altimeter synthetic T/S profiles (thin blue) and the RAPID array (thin dark green), with the 1-year lowpass filtered time series showing the interannual variations of the MHT from altimeter (thick blue), the RAPID array (thick dark green), and the energy budget (thick orange).

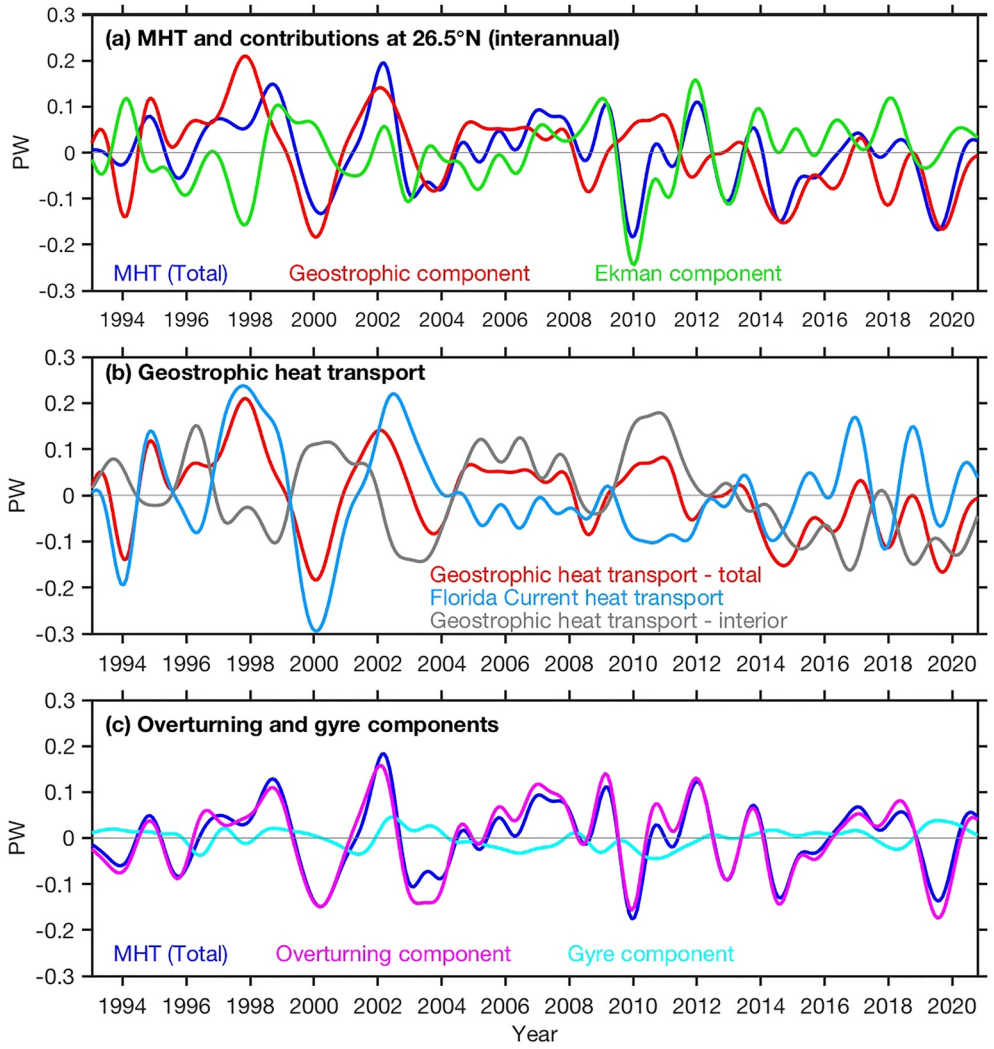

Figure 10. Interannual variations of the altimetry-derived (a) MHT (blue) and contributions from the geostrophic (red) and Ekman (green) components at 26.5°N, (b) the total geostrophic heat transport (red), the geostrophic heat transports from the Florida Current (light blue) and the interior region (gray), and (c) the MHT (blue) and contributions from the overturning (magenta) and gyre (cyan) components.

the Q_{geo} into heat transport across the Florida Straits and the interior region (Figure 10b) indicates that the decreasing trend in the Q_{geo} comes from the interior region, and that there is no trend in the heat transport by the Florida Current. Before 2004, large variability in the Florida Current transport dominates the total geostrophic heat transport, while from 2004 through 2015 the interior geostrophic transport plays a more important role. This changing dominance can be explained by the reduced anomalies in the Q_{FC} since 2004, dominated by the anomalous volume transport. Florida Current transport has been the subject of numerous studies (Hirschi et al., 2019 and references therein) and its variability has been attributed to changes in the surface wind stress curl and in the Loop Current. Our preliminary analysis also suggests a strong link between local meridional winds and the strength of the Florida Current transport. Detailed analysis of various forcing is the subject of our ongoing study. It is also interesting to note that the heat transports by the Florida Current and interior region compensate each other, that is, they are negatively correlated with a correlation coefficient of −0.65. This is not surprising as the Florida Current is the main return flow of the wind-driven interior gyre circulation.

Both the Ekman and geostrophic heat transports are correlated with North Atlantic Oscillation (NAO). The Ekman heat transport is positively correlated with NAO ($r = 0.62$), whereas the geostrophic heat transport

is negatively correlated with NAO ($r = -0.45$), both exceeding the 95% significance level of 0.37. However, because of the compensation between the Ekman and geostrophic heat transports, there is no significant correlation between the total MHT and NAO. Due to the relatively stronger role of the Ekman heat transport during the RAPID period, the total MHT shows a moderate correlation ($r = 0.50$) with NAO.

Similar to the seasonal changes, separating the MHT into overturning and gyre contributions indicates that the overturning component dominates the interannual variations in the MHT (Figure 10c), explaining about 91% of the total interannual variability in MHT. Variations in the volume transport accounts for 90% of the overturning component. In contrast, the interannual variations of the gyre component is mainly due to changes in the temperature deviations from the zonal average, which explains 84% of the total variance in Q_{gyre}. In terms of regional contributions, the Q_{FC} accounts for about 80% of the total interannual variance in Q_{gyre}, with the remaining 20% coming from the interior region. The gyre component is negatively correlated with the overturning component, though the correlation is somewhat low ($r = -0.43$), suggesting that Q_{gyre} acts to partly compensate for the interannual variations in the Q_{ot}.

4.2. South Atlantic

4.2.1. Time-Mean

The time-mean MHT at all four latitudes are comparable, varying between 0.57 ± 0.21 PW to 0.66 ± 0.16 PW (mean ± STD), with a slight increase from 34.5°S to 25°S (Table 1). These altimeter-derived mean values are about 0.1–0.2 PW higher than the mean MHT values from the energy budget by Trenberth et al. (2019). The geostrophic heat transport shows a large increase toward north from 0.40 ± 0.16 PW at 34.5°S to 1.19 ± 0.09 PW at 20°S, whereas the Ekman heat transport decreases significantly northward from 0.17 ± 0.20 at 34.5°S to −0.57 ± 0.14 PW at 20°S, compensating the increase in the geostrophic heat transport. Same as in the North Atlantic, the overturning component dominates the total MHT at all four latitudes. However, unlike at 26.5°N where the gyre component contributes positively to the net northward heat transport, the gyre components at all four latitudes are negative, partly compensating the northward MHT from the overturning circulation. The negative gyre component is attributed to the southward flowing Brazil Current at the western boundary, which transports warm water poleward. The Q_{gyre} is roughly the same from 25°S to 34.5°S, around −0.17 ± 0.03 PW, but much smaller at 20°S, about −0.06 ± 0.02 PW, due to weak, eddy-dominated Brazil Current at this location (e.g., Goes et al., 2019; Soutelino et al., 2011). The weak northward return flow linked to the weak gyre circulation at 20°S also contributes to the smaller Q_{gyre} at this location. Different from the North Atlantic at 26.5°N where the Q_{gyre} in the interior region switches sign between the western and eastern half of the basin from southward to northward, in the South Atlantic the Q_{gyre} are southward throughout the basin. This perhaps explains the relatively stronger Q_{gyre} in the South Atlantic.

4.2.2. Seasonal Cycle

The phase of the MHT seasonal variations (monthly averages) at the four latitudes from 20°S to 34.5°S are coherent, with their maxima in April–May and minima in August–November (Figure 11), but the amplitude decreases northward from 0.45 ± 0.04 PW at 34.5°S to 0.29 ± 0.03 PW at 20°S. The error bar here is one standard error. The seasonal variation accounts for more than half of the total variance in MHT at 30°S (54%) and 34.5°S (53%), and accounts for 31% of the total variance in MHT at 20°S and 25°S. The seasonal variations of the MHT from the energy budget also experience high values around April to June and low values around October to December, but their amplitudes are nearly equal at different latitudes and are much stronger (roughly twice) than these from altimeter estimates, particularly at 20°S and 25°S.

The contributions from both the geostrophic and Ekman transports also show a northward decrease in the amplitude of seasonal variation (Table 1). At 20°S and 25°S, the amplitudes of seasonal variation from the geostrophic and Ekman transports are comparable, around 0.20 ± 0.02 PW, and they work together to strengthen the seasonal cycle in the total MHT. The amplitude of the seasonal variation in Q_{ekm} increases to 0.38 ± 0.03 PW at 30°S and 0.48 ± 0.03 PW at 34.5°S, and the amplitude in Q_{geo} is about 0.10 PW weaker than that in Q_{ekm}. The maximum Q_{geo} occurs one month before the peak in the total heat transport, whereas the maximum Q_{ekm} occurs one month after the peak in the total MHT.

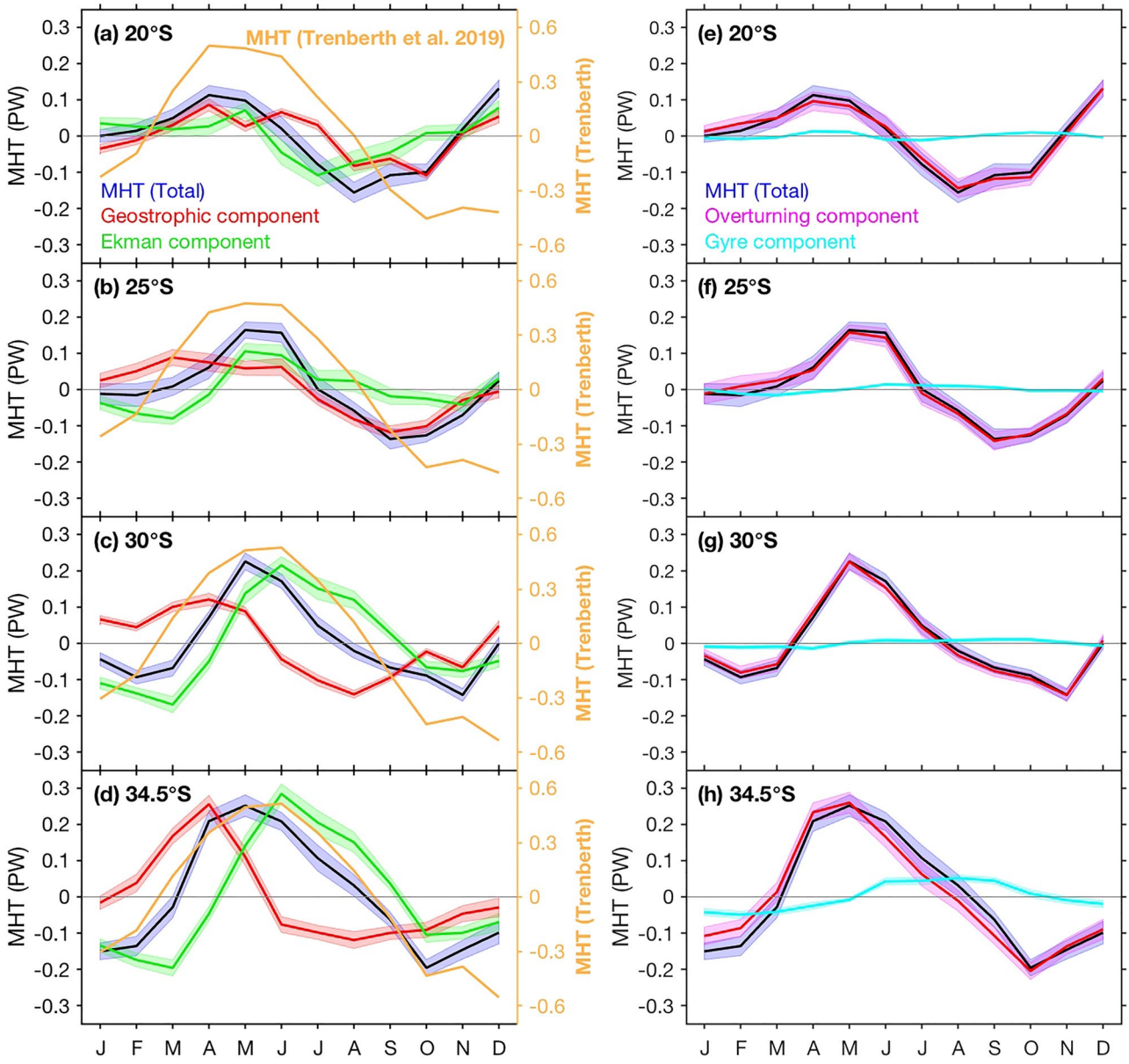

Figure 11. Seasonal variations of the altimeter-based MHT (blue) and contributions from the geostrophic (red) and Ekman (green) components at (a) 20°S, (b) 25°S, (c) 30°S, and (d) 34.5°S. Also shown is the seasonal variation of the MHT from the energy budget (orange, right axis). Panels (e–h) are similar to (a–d), but for contributions of the overturning (magenta) and gyre (cyan) components to the total MHT seasonal variations. Shading around each curve indicates two standard errors.

Examination of the overturning and gyre contributions shows that the overturning component dominates the seasonal cycle in MHT at all four latitudes, which is mainly due to seasonal changes in volume transport. Although the gyre component contributes moderately to the mean MHT except at 20°S, its contribution to the seasonal variations in MHT is negligible except at 34.5°S, where its peak-to-peak amplitude (0.10 ± 0.01 PW) is comparable to that at 26.5°N. Similar to 26.5°N, the temperature deviations from the zonal average dominate the seasonal signal in Q_{gyre}, accounting for 87% of its seasonal variance, the reminder 13% is contributed by the changes in the velocity deviations from the zonal average.

4.2.3. Interannual Variations

Unlike the southward strengthening of the seasonal variations in the MHT from 20°S to 34.5°S, the interannual variations in the MHT at 20°S and 25°S are stronger than the variations at 30°S and 34.5°S (Figure 12).

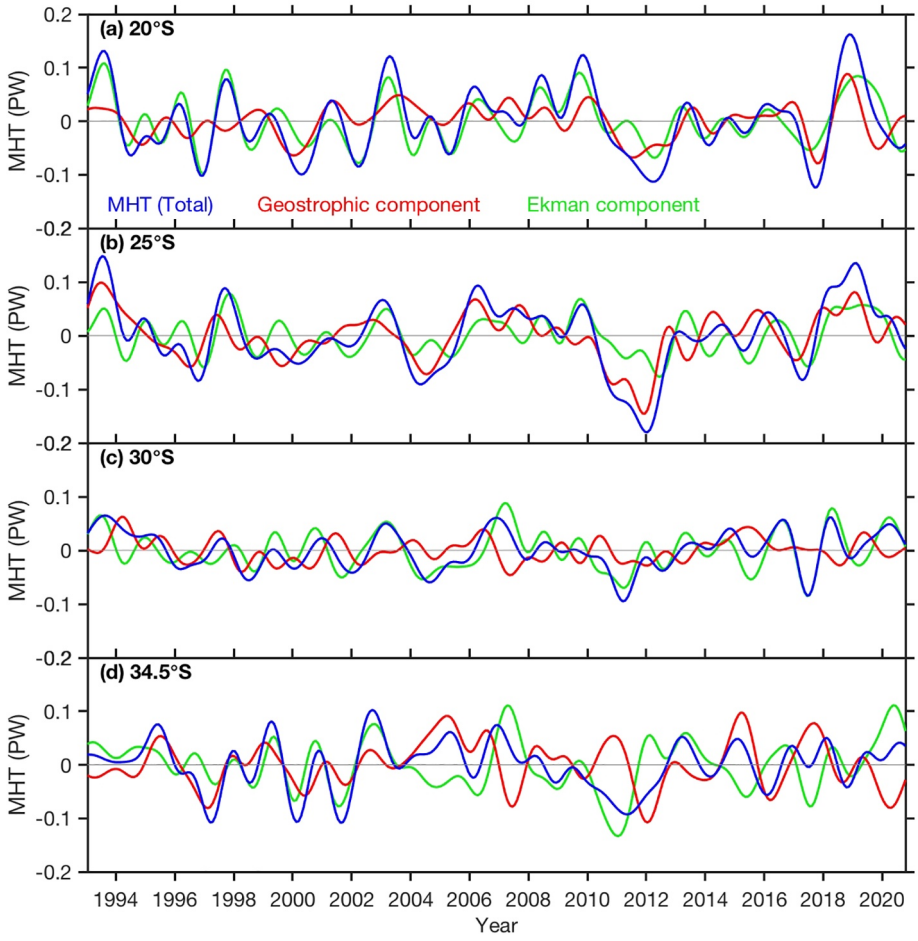

Figure 12. Interannual variations of the altimeter-based MHT (blue) and contributions from the geostrophic (red) and Ekman (green) components at (a) 20°S, (b) 25°S, (c) 30°S, and (d) 34.5°S.

The weak variability at 30°S is mainly due to weak variations in the geostrophic component. The variabilities in Q_{geo} and Q_{ekm} at 34.5°S are comparable to those at 20°S and 25°S, however, given that during 65% of the record these two components have opposite signs, they act to partly compensate one another. This suggests that the geostrophic and Ekman heat transports at this latitude work against each other, which consequently weakens the variability in the total MHT. In contrast, at 20°S and 25°S more than half the time (55%) Q_{geo} and Q_{ekm} are compounded and work together to strengthen the MHT variability. Similar to the North Atlantic, the dominance of the geostrophic and Ekman transports on the total MHT varies with time. For example, at 34.5°S, the geostrophic transport dominates during 1995–1997, 2004–2005, and 2014–2018, and the Ekman transport plays a dominant role during 2002–2003 and 2009–2011.

In terms of the contributions from the overturning and gyre components (Figure 13), at all four latitudes the interannual variations in the MHT are dominated by the overturning component, which accounts for 97% of the total interannual variance in the MHT at 20°S and 25°S, and more than 80% at 30°S and 34.5°S. The interannual variations in Q_{ot} are largely controlled by changes in the volume transport, which explains more than 90% of the total variance in Q_{ot} at all four latitudes. The interannual variations in the Q_{gyre} are very weak and negligible at 20°S and 25°S. Although the gyre contribution to the total MHT interannual variability at 30°S and 34.5°S is still small compared to the overturning component, it is not negligible and sometimes the anomalies in Q_{gyre} can be as large as anomalies in Q_{ot}. Figure 13 shows that Q_{gyre} tends to work against Q_{ot} in terms of contributing to the total variability of the MHT. The increased Q_{gyre} toward south is induced by the intensification of the southward-flowing Brazil Current at the western boundary and the northward-flowing Benguela Current at the eastern boundary (e.g., Peterson & Stramma, 1991).

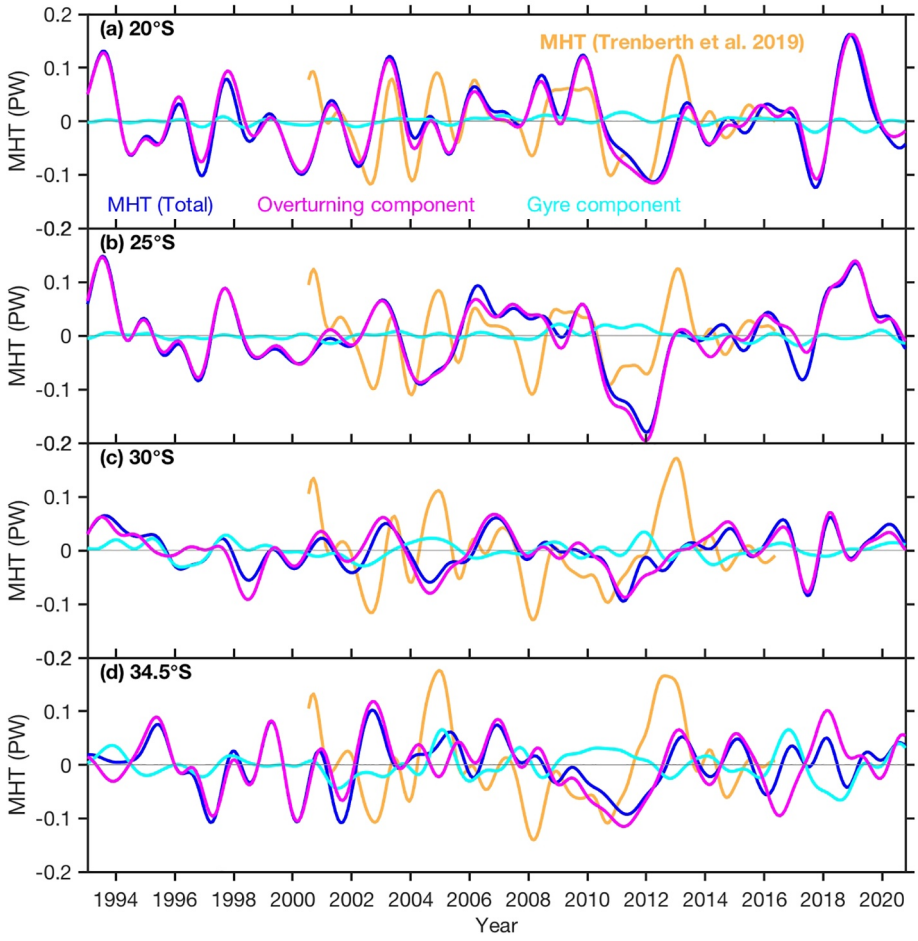

Figure 13. Interannual variations of the altimeter-derived MHT (blue) and contributions from the overturning (magenta) and gyre (cyan) components at (a) 20°S, (b) 25°S, (c) 30°S, and (d) 34.5°S. Also shown is the interannual variations of the MHT derived from the energy budget (Orange curves).

Another potential contributor to the stronger Q_{gyre} to the south, particularly at 34.5°S, is the Agulhas rings shed from the Agulhas Current retroflection (e.g., Richardson, 2007).

Different from the results at 26.5°N where the MHT interannual variations from our estimates and from the energy budget show good agreement ($r = 0.65$), in the South Atlantic Ocean we only found statistically significant correlation between the two estimates at 20°S with a correlation $r = 0.60$ (95% significance 0.48). The correlations at other three latitudes are quite low (Figure 13). This southward decrease in correlation is probably due in part to the accumulation of errors in the energy budget as it moves farther away from the North Pole, since the MHT at each latitude was estimated by integrating the net surface heat flux and changes in ocean heat content from that latitude to the North Pole, particularly considering the large uncertainties in the ocean heat content changes in the South Atlantic Ocean (Dong et al., 2020). Interestingly, the heat transport convergence ($MHT_{34.5S}$–MHT_{20S}) from the two estimates agree well with correlation $r = 0.71$ (Figure 14), suggesting that our estimates capture the changes in heat content and air-sea heat fluxes in this region. We note that the heat transport convergence for the energy budget is taken as the difference between 33.5°S (the southern most estimates available) and 20°S. Further studies are needed to investigate the possible causes for the differences in MHT estimates.

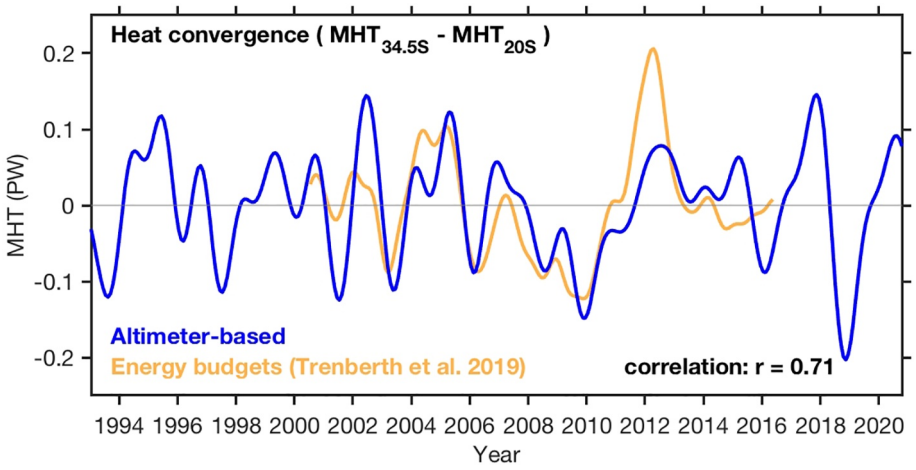

Figure 14. Interannual variations of the oceanic heat convergence in the subtropical South Atlantic ($MHT_{34.5°S}$-$MHT_{20°S}$) from altimeter-derived estimates (blue) and the energy budget (orange).

5. Discussion

We have shown that the MHT estimates in the North Atlantic at 26.5°N from all three methods (RAPID array, energy budget by Trenberth et al., 2019, and our altimeter-based estimates) agree well on interannual time series. However, their seasonal variations differ considerably. A breakdown of the transports into various contributions indicates that the difference in the seasonality between the results from the RAPID array and our altimeter-based estimates arises from the geostrophic volume transport in the interior region between the Bahamas to Africa integrated from the surface down to the overturning depth (V_{int}). As shown in Figure 15a, the seasonal variations relative to the annual mean in the V_{int} from RAPID are dominated by the strong positive anomalies in October and November close to 3.9 Sv, with weaker positive anomalies during September and December about 0.5 Sv and negative anomalies from January to August about −1.0 Sv. Our estimates from altimeter show positive anomalies from December to May and negative anomalies from June to November, with the maximum of 2.4 Sv in March and minimum of −2.9 Sv in August. Interestingly, the seasonal variations of the interior transport from RAPID moorings match their dynamic height differences between the eastern and western boundary, whereas the seasonal variations in our interior transport estimates match the SSH difference between the two boundaries (Figure 15a). The dynamic heights for the RAPID are calculated from the temperature and salinity profiles at each boundary. However, because most of the RAPID profiles do not have measurements shallower than 100 m depth due to the design of moorings to prevent high loss rates associated with the surface expression (McCarthy et al., 2015), the difference shown in Figure 15a is taken at 100 m depth, the shallowest depth where there are at least three years of data available at each boundary to construct seasonal cycle.

A number of studies (Chidichimo et al., 2010; Kanzow et al., 2010; Velez-Belchi et al., 2017; Zhao & Johns, 2014) have investigated the seasonal cycle in the AMOC at 26.5°N from the RAPID array and found that it is largely controlled by the density changes at the eastern boundary. Indeed, examination of the dynamic height (at 100 m depth) at each boundary (Figure 15b) demonstrates that the dynamic height changes at the eastern boundary dominate the east-west difference on seasonal time scale, particularly the strong positive anomalies during October to December. However, the altimeter SSH at both the eastern and western boundary show large variations, with somewhat stronger variations at the western boundary (Figure 5c). In fact, satellite-altimetry observations reveal that SSH variability at seasonal timescales account for the majority of total SSH variance west of 60°W (Domingues et al., 2016). As a result, the SSH at the western boundary plays a larger role in the SSH difference between the two boundaries, except in November and December when the large SSH anomalies at the eastern boundary dominates. This is consistent with Longworth et al. (2011) who found that the contributions from the western boundary to the transport anomalies at 26.5°N are stronger than those from the eastern boundary on both seasonal and interannual time scales. We also computed the dynamic heights at both boundaries from the WOA18 temperature and

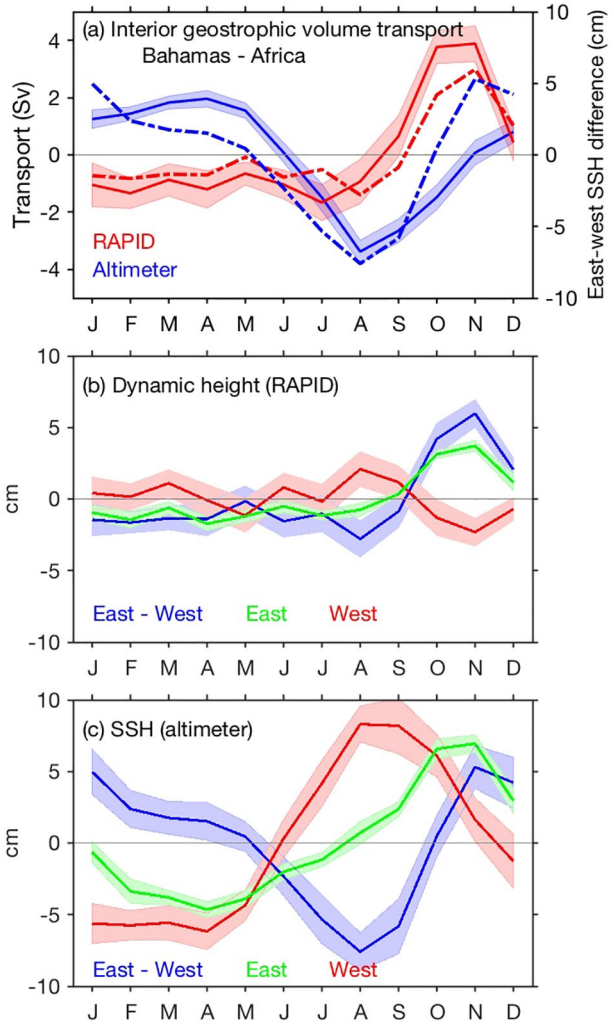

Figure 15. Monthly climatology of the geostrophic volume transport in the interior ocean from the Bahamas to Africa, integrated from the sea surface down to the depth of overturning (V_{int} ~ 1,000 m) from the RAPID array (red) and the altimeter-based estimates (blue). The dashed lines are east-west dynamic height difference from RAPID moorings (red, at 100 m depth) and SSH difference from altimeter (blue). (b) Dynamic height at the eastern (green) and western (red) boundaries and their difference (blue) from RAPID data at 100 m depth. (c) SSH from altimeter at the eastern (green) and western (red) boundaries and their difference (blue). The shading around each curve indicates two standard errors.

salinity monthly climatology (not shown), and their seasonal changes are very similar to the variations shown in the SSH.

As mentioned earlier, the RAPID moorings do not sample the upper 100 m water column where the seasonal variations are primarily contained. Although extrapolating the profiles to the surface with cubic terms has greatly reduced the errors in transport estimates compared to the linear extrapolation (McCarthy et al., 2015), how much this extrapolation contributes to the discrepancy of the seasonal cycle in the interior transports is still unclear and requires further investigation. Kanzow et al. (2010) and Zhao and Johns (2014) attributed the seasonal variations in the interior transport from RAPID to the local wind forcing near the eastern boundary. However, Velez-Belchi et al. (2017) argued that the linear Rossby wave model used in those studies cannot explain the AMOC seasonal variation because the results are very sensitive to the choice of the zonal range of the wind stress curl. A better understanding of the forcing mechanisms for the seasonal variations in the interior transport can also help to diagnose the discrepancy from different estimates. This is another area that needs further investigation.

Previous studies suggested coherent interannual changes in MHT in the Atlantic Ocean between the equator and 45°N from energy budget (Trenberth et al., 2019) and between 35°S and 40°N from an inverse model (Kelly et al., 2014). Lead-lag correlation analysis of the altimeter-derived MHT during 1993–2020, however, does not show a significant correlation of MHT at 26.5°N with these in the subtropical South Atlantic (20°S–34.5°S), although a maximum correlation around 0.3 was found when MHT at 26.5°N leads by about a year. These observations therefore indicate that MHT coherence between South and North Atlantic is not evident at interannual timescales, which are likely dominated by local variability inherent to each basin. Longer records will enable assessing meridional coherency in decadal and longer timescales.

While interannual MHT variability appears decoupled between the South and North Atlantic, within the South Atlantic, the MHT estimates at 20°S, 25°S, and 30°S are correlated with each other near zero lag with correlations ranging from 0.51 to 0.79 (95% significance 0.37; Figure 16). However, their correlations with the MHT at 34.5°S are somewhat lower, and this correlation increases with decreasing distance, from 0.30 between 20°S and 34.5°S to 0.41 between 30°S and 34.5°S. Interestingly, the analysis during the overlapping time period (2000–2016) of altimeter and energy budget shows higher cross-correlation among the four latitudes for the altimeter-derived estimates, ranging from 0.61 to 0.82 (95% significance 0.48), with MHT at 34.5°S leading by 3 to 9 months. High correlations between different latitudes are also seen for the MHT estimates from energy budget but at zero lag (Figure 16). The higher correlations in the altimeter-derived MHT during 2000–2016 is likely driven by the coherent negative anomalies advected from the south during 2009–2012. However, the reason for the short-time northward propagation is unclear and requires further investigation.

In the South Atlantic, daily MOC has been estimated using in situ observations from pressure-equipped inverted echo sounder (PIES) moorings at 34.5°S (Kersalé et al., 2020; Meinen et al, 2013, 2018), though MHT estimates from these PIES are not yet available at this time. The altimeter-derived MOC at this latitude (18.32 Sv) is somewhat stronger than those estimated from PIES moorings (14.7 Sv from the two shallowest moorings by Meinen et al. [2018] and 17.3 Sv from nine moorings by Kersalé et al. [2020]), but the differences are within the error estimates of 5.0 Sv (Kersalé et al., 2020). However, the MOC variability from PIES moorings, 5.40 Sv from Meinen et al. (2018) and 11.25 Sv from Kersalé et al. (2020), are much stronger even

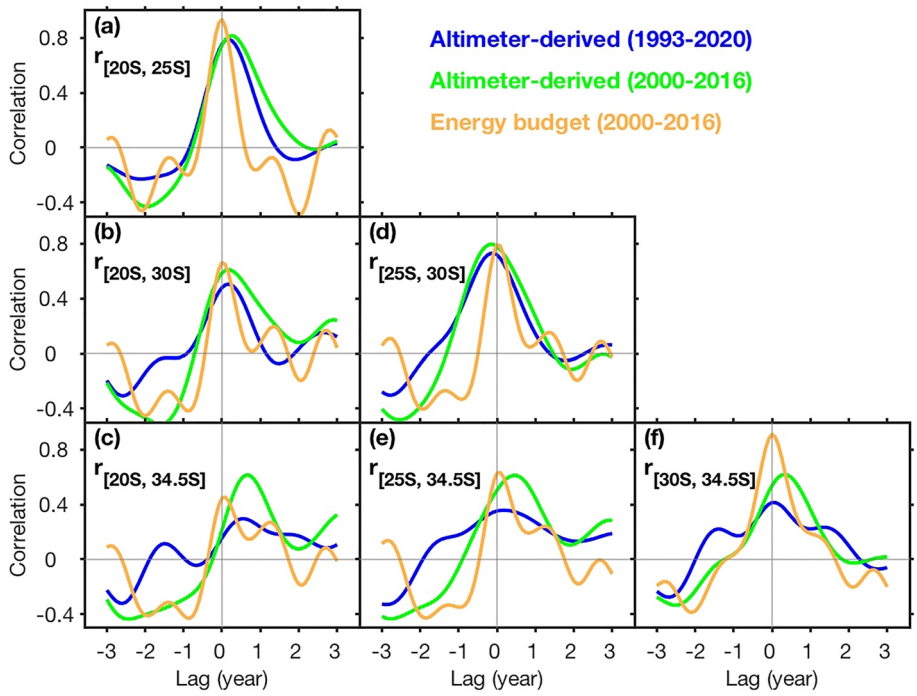

Figure 16. Lead-lag correlations of MHT estimates between (a) 20°S and 25°S, (b) 20°S and 30°S, (c) 20°S and 34.5°S, (d) 25°S and 30°S, (e) 25°S and 34.5°S, and (f) 30°S and 34.5°S. Negative lags correspond to MHT to the north leading MHT to the south, and vice versa. Blue and green curves are for the altimeter-derived MHT during 1993–2020 and 2000–2016, respectively, and orange curves are for the energy budget estimates from Trenberth et al. (2019) during 2000–2016.

with the monthly averages compared to the 3.19 Sv from altimeter-based estimates during their overlapping time period (September 2013 to April 2017). Because of its large variability and short time period, MOC seasonal variations from PIES estimates are not yet as robust as those estimated from longer time series (Kersalé et al., 2020). Nevertheless, the semi-annual signal in MOC estimates from altimeter is not as strong as suggested by PIES estimates. The less than 4-years overlapping time period is also too short for a meaningful comparison of MOC interannual variations between PIES and altimeter-derived estimates, given the 95% significance of 0.98. Longer overlapping time series are necessary to understand the difference between those estimates and for potential improvements in MOC and MHT estimates in the South Atlantic.

6. Summary

By merging conventional oceanographic observations with those obtained from satellites, we are able to estimate the MOC and MHT at multiple latitudes in the Atlantic Ocean since 1993. The overturning depth varies from 1,000 m at 26.5°N to 1,200 m at 34.5°S, and that the MHT is highly correlated with the MOC at each latitude from 26.5°N to 34.5°S, with correlations varying from $r = 0.89$ to $r = 0.96$. Linear transfer coefficients further indicate that the response of MHT to MOC is similar at the different latitudes, with a 1 Sv increase in MOC resulting in an increase in MHT of 0.064 ± 0.012 PW, 0.069 ± 0.012 PW, 0.074 ± 0.008 PW, 0.067 ± 0.012 PW, and 0.056 ± 0.008 PW at 26.5°N, 20°S, 25°S, 30°S, and 34.5°S, respectively. In addition, the geostrophic heat transport shows a slightly weaker response to the volume transport compared to the total MHT, whereas the Ekman heat transport is much more sensitive to the volume transport due to the warmer water at the surface layer.

At 26.5°N, the mean MHT from our estimates is 1.09 ± 0.21 PW, slightly lower than that from the RAPID array (1.20 ± 0.28 PW) due to a weaker geostrophic transport. The total MHT is largely dominated by the overturning component, which accounts for 89% of the total MHT, with the remainder 11% coming from the gyre component. Although there are differences between our estimates and the RAPID results in terms

of seasonal variations, good agreement is observed on interannual timescales. Both the geostrophic and Ekman components contribute significantly to the MHT changes on seasonal and interannual time scales, and their dominance changes with time. The geostrophic component plays a dominant role in the MHT interannual variations during 1993–2004 due to large variability in the Florida Current transport, whereas the Ekman component dominates MHT changes during 2005–2014. This suggests the importance of monitoring both wind and density fields to capture the MHT changes. Our results also suggest a negative correlation between the geostrophic and Ekman heat transports, suggesting they partly compensate each other to weaken the total MHT variability. Over the past 28 years, the MHT shows strong positive anomalies (>1 STD) during 1998, 2001/2002, 2007, 2009, and 2011/2012, and negative anomalies (<−1 STD) during 1995, 1999/2000, 2003, 2009/2010, 2012, 2014, and 2019. These large anomalies could have an impact on regional sea level and rainfall patterns, which are subjects of future studies.

In the South Atlantic, the MHT shows the strongest variability at 34.5°S, but more than half of its total variability is accounted for by the seasonal variations. The amplitude of the MHT seasonal cycle increases southward from 0.29 ± 0.03 PW at 20°S to 0.45 ± 0.04 PW at 34.5°S. On interannual time scale, the MHT at 20°S and 25°S experiences larger variations than that at 30°S and 34.5°S, in part due to the fact that the geostrophic and Ekman components work together to strengthen the MHT variability, but they tend to work against each other to weaken the MHT variability at 30°S and 34.5°S. Similar to the North Atlantic, both the geostrophic and Ekman transports contribute significantly to the total MHT on both the seasonal and interannual time scales. On interannual time scale, the geostrophic and Ekman heat transports dominate the total MHT during different time periods. Although the large anomalies in MHT do not always occur at the same time between 20°S and 34.5°S, positive anomalies (>1 STD) can be seen during 2002/2003 and 2006, and negative anomalies (<−1 STD) during 2009–2012. These anomalies propagate northward from 34.5°S and are similarly observed at 20°S after 9 months. Interestingly, the MHT estimates show large positive anomalies during 2018–2019 at 20°S and 25°S, but not at 30°S and 34.5°S, suggesting a large heat divergence in the subtropical South Atlantic. A preliminary examination of ocean heat content from the World Ocean Database indicates that the decrease in heat content in the region cannot fully account for the heat divergence, implying anomalous heat input from the atmosphere. Detailed analysis will be explored in the future.

Although further investigations are required to address the discrepancies in the seasonal variations of the geostrophic transport, a longer time series will help to better understand the variability of the MOC and MHT on interannual to decadal time scales and their forcing mechanisms. With continuing effort in the science community to develop different methods to estimate the MOC and MHT, it is expected that the comparison of those results will help to optimize the observing system and to derive more accurate estimates. The methodology presented here to compute the MOC and MHT using synthetic T/S profiles derived from altimeter and in situ measurements demonstrated the importance of integrating observations from different observing platforms to extract information which are not readily available from a single observing component. The methodology also provides a means to estimate the MOC and MHT in near real time, and can be used to validate ocean models, to detect climate variability, and to investigate its impact on extreme weather events. Finally, observations analyzed and presented here may be leveraged to verify/validate model simulations.

Data Availability Statement

This research was carried out in part under the auspices of the Cooperative Institute for Marine and Atmospheric Studies, a Cooperative Institute of the University of Miami and the National Oceanic and Atmospheric Administration, cooperative agreement #NA20OAR4320472. Satellite altimetry products were produced by the Copernicus Marine and Environment Monitoring Service (CMEMS) and can be found at https://marine.copernicus.eu/about/producers/sl-tac. NOAA's High Resolution OISST is available at: https://psl.noaa.gov/data/gridded/data.noaa.oisst.v2.highres.html. The Florida Current transport from the submarine cable is available at http://www.aoml.noaa.gov/phod/floridacurrent/. Data from the RAPID AMOC monitoring project is funded by the Natural Environment Research Council and are freely available from www.rapid.ac.uk/rapidmoc. XBT data along AX07 and AX18 can be found at https://www.aoml.noaa.gov/phod/hdenxbt/index.php. The MHT from the RAPID array can be found at

https://mocha.rsmas.miami.edu/results/index.html, and the MHT estimates from Trenberth et al. (2019) energy budget were downloaded from https://dashrepo.ucar.edu/dataset/Ocean_MHT_Values.html. The monthly North Atlantic Oscillation index from NOAA's National Weather Service is available at https://www.cpc.ncep.noaa.gov/products/precip/CWlink/pna/nao.shtml.

Acknowledgments
We would like to express our appreciation to R. Perez and two anonymous reviewers for helpful comments, and support from the NOAA Atlantic Oceanographic and Meteorological Laboratory. We also acknowledge additional support from NOAA Climate Variability Program (GC16-210) and NOAA Global Ocean Monitoring and Observing program under the XBT project and State of the Climate: Quarterly Report on the Meridional Heat Transport in the Atlantic Ocean project.

References

Baringer, M. O. N., & Larsen, J. C. (2001). Sixteen years of Florida Current Transport at 27°N. *Geophysical Research Letters*, *28*(16), 3179–3182. https://doi.org/10.1029/2001gl013246

Böning, C. W., Dieterich, C., Barnier, B., & Yanli Jia, Y. L. (2001). Seasonal cycle of meridional heat transport in the subtropical North Atlantic: A model intercomparison in relation to observations near 25°N. *Progress in Oceanography*, *48*, 231–253. https://doi.org/10.1016/s0079-6611(01)00006-4

Buckley, M. W., & Marshall, J. (2016). Observations, inferences, and mechanisms of the Atlantic meridional overturning circulation: A review. *Reviews of Geophysics*, *54*, 5–63. https://doi.org/10.1002/2015RG000493

Chidichimo, M. P., Kanzow, T., Cunningham, S. A., Johns, W. E., & Marotzke, J. (2010). The contribution of eastern-boundary density variations to the Atlantic meridional overturning circulation at 26.5°N. *Ocean Science*, *6*, 475–490. https://doi.org/10.5194/os-6-475-2010

Domingues, R., Baringer, M., & Goni, G. (2016). Remote sources for year-to-year changes in the seasonality of the Florida Current transport. *Journal of Geophysical Research: Oceans*, *121*(10), 7547–7559. https://doi.org/10.1002/2016jc012070

Domingues, R., Goni, G., Baringer, M., & Volkov, D. (2018). What caused the accelerated sea level changes along the United States East Coast during 2010-2015?. *Geophysical Research Letters*, *45*(24), 13367–13376. https://doi.org/10.1029/2018GL081183

Dong, S., Goni, G., & Bringas, F. (2015). Temporal variability of the South Atlantic meridional overturning circulation between 20°S and 35°S. *Geophysical Research Letters*, *42*, 7655–7662. https://doi.org/10.1002/2015GL065603

Dong, S., Lopez, H., Lee, S.-K., Meinen, C. S., Goni, G. J., & Baringer, M. O. (2020). What caused the large-scale heat deficit in the subtropical South Atlantic Ocean during 2009–2012?. *Geophysical Research Letters*, *47*(11), e2020GL088206. https://doi.org/10.1029/2020gl088206

Drijfhout, S., van Oldenborgh, G. J., & Cimatoribus, A. (2012). Is a decline of AMOC causing the warming hole above the North Atlantic in observed and modeled warming patterns?. *Journal of Climate*, *25*(24), 8373–8379. https://doi.org/10.1175/JCLI-D-12-00490.1

Duchez, A., Courtois, P., Harris, E., Josey, S. A., Kanzow, T., Marsh, R., et al. (2016). Potential for seasonal prediction of Atlantic sea surface temperatures using the RAPID array at 26°N. *Climate Dynamics*, *46*, 3351–3370. https://doi.org/10.1007/s00382-015-2918-1

Frajka-Williams, E., Ansorge, I. J., Baehr, J., Bryden, H. L., Chidichumo, M. P., Cunningham, S. A., et al. (2019). Atlantic meridional overturning circulation: Observed transport and variability. *Frontiers in Marine Science*, *6*, 260. https://doi.org/10.3389/fmars.2019.00260

Goes, M., Christophersen, J., Dong, S., Goni, G., & Baringer, M. O. (2018). An updated estimate of salinity for the Atlantic Ocean sector using temperature-salinity relationships. *Journal of Atmospheric and Oceanic Technology*, *35*, 1771–1784. https://doi.org/10.1175/JTECH-D-18-0029.1

Goes, M., Cirano, M., Mata, M. M., & Majumder, S. (2019). Long-term monitoring of the Brazil current transport at 22°S from XBT and altimetry data: Seasonal, interannual, and extreme variability. *Journal of Geophysical Research: Oceans*, *124*, 3645–3663. https://doi.org/10.1029/2018JC014809

Goni, G., DeMaria, M., Knaff, J., Sampson, C., Ginis, I., Bringas, F., et al. (2009). Applications of satellite-derived ocean measurements to tropical cyclone intensity forecasting. *Oceanography*, *22*(3), 190–197. https://doi.org/10.5670/oceanog.2009.78

Goni, G., Kamholz, S., Garzoli, S., & Olson, D. (1996). Dynamics of the Brazil-Malvinas confluence based on inverted echo sounders and altimetry. *Journal of Geophysical Research*, *101*(C7), 16273–16289. https://doi.org/10.1029/96jc01146

Hall, M. M., & Bryden, H. L. (1982). Direct estimates and mechanisms of ocean heat transport. *Deep-Sea Research Part A. Oceanographic Research Papers*, *29*, 339–359. https://doi.org/10.1016/0198-0149(82)90099-1

Hirschi, J. J.-M., Frajka-Williams, E., Blaker, A. T., Sinha, B., Coward, A., Hyder, P., et al. (2019). Loop current variability as trigger of coherent gulf stream transport anomalies. *Journal of Physical Oceanography*, *49*, 2115–2132. https://doi.org/10.1175/jpo-d-18-0236.1

Hobbs, W. R., & Willis, J. K. (2012). Midlatitude North Atlantic heat transport: A time series based on satellite and drifter data. *Journal of Geophysical Research*, *117*, C01008. https://doi.org/10.1029/2011JC007039

Jayne, S. R., & Marotzke, J. (2001). The dynamics of ocean heat transport variability. *Reviews of Geophysics*, *39*, 385–411. https://doi.org/10.1029/2000rg000084

Johns, W. E., Baringer, M. O., Beal, L. M., Cunningham, S. A., Kanzow, T., Bryden, H. L., et al. (2011). Continuous, array-based estimates of Atlantic Ocean heat transport at 26.5°N. *Journal of Climate*, *24*, 2429–2449. https://doi.org/10.1175/2010JCLI3997.1

Kanzow, T., Cunningham, S. A., Johns, W. E., Hirschi, J. J.-M., Marotzke, J., Baringer, M. O., et al. (2010). Seasonal variability of the Atlantic meridional overturning circulation at 26.5°N. *Journal of Climate*, *23*, 5678–5698. https://doi.org/10.1175/2010JCLI3389.1

Katsumata, K., & Yoshinari, H. (2010). Uncertainties in global mapping of Argo drift data at the parking level. *Journal of Oceanography*, *66*, 553–569. https://doi.org/10.1007/s10872-010-0046-4

Kelly, K. A., Thompson, L., & Lyman, J. (2014). The coherence and impact of meridional heat transport anomalies in the Atlantic Ocean inferred from observations. *Journal of Climate*, *27*, 1469–1487. https://doi.org/10.1175/jcli-d-12-00131.1

Kersalé, M., Meinen, C. S., Perez, R. C., Le Hénaff, M., Valla, D., Lamont, T., et al. (2020). Highly variable upper and abyssal overturning cells in the South Atlantic. *Science Advances*, *6*(32), eaba7573. https://doi.org/10.1126/sciadv.aba7573

Kostov, Y., Armour, K. C., & Marshall, J. (2014). Impact of the Atlantic meridional overturning circulation on ocean heat storage and transient climate change. *Geophysical Research Letters*, *41*, 2108–2116. https://doi.org/10.1002/2013GL058998

Lebedev, K., Yoshinari, H., Maximenko, N. A., & Hacker, P. W. (2007). YoMaHa'07: Velocity data assessed from trajectories of Argo floats at parking level and at the sea surface. *IPRC Technical Note No*, *4*(2), 16.

Little, C. M., Piecuch, C. G., & Ponte, R. M. (2017). On the relationship between the meridional overturning circulation, alongshore wind stress, and United States East Coast sea level in the community earth system model large ensemble. *Journal of Geophysical Research: Oceans*, *122*, 4554–4568. https://doi.org/10.1002/2017JC012713

Longworth, H. R., Bryden, H. L., & Baringer, M. O. (2011). Historical variability in Atlantic meridional baroclinic transport at 26.5°N from boundary dynamic height observations. *Deep Sea Research Part II: Topical Studies in Oceanography*, *58*, 1754–1767. https://doi.org/10.1016/j.dsr2.2010.10.057

Lopez, H., Dong, S., Lee, S.-K., & Goni, G. (2016). Decadal modulations of interhemispheric global atmospheric circulations and monsoons by the South Atlantic meridional overturning circulation. *Journal of Climate*, *29*(5), 1831–1851. https://doi.org/10.1175/JCLI-D-15-0491.1

Lorbacher, K., Dengg, J., Böning, C. W., & Biastoch, A. (2010). Regional patterns of sea level change related to interannual variability and multidecadal trends in the Atlantic meridional overturning circulation. *Journal of Climate*, *23*(15), 4243–4254. https://doi.org/10.1175/2010JCLI3341.1

Lozier, M. S. (2012). Overturning in the North Atlantic. *Annual Review of Marine Science*, *4*, 291–315. https://doi.org/10.1146/annurev-marine-120710-100740

Lozier, M. S., Li, F., Bacon, S., Bahr, F., Bower, A.S., Cunningham, S. A., et al. (2019). A sea change in our view of overturning in the subpolar North Atlantic. *Science*, *363*, 516–521. https://doi.org/10.1126/science.aau6592

Majumder, S., Schmid, C., & Halliwell, G. (2016). An observations and model-based analysis of meridional transports in the South Atlantic. *Journal Geophysical Research: Oceans*, *121*, 5622–5638. https://doi.org/10.1002/2016JC011693

Marshall, J., Armour, K. C., Scott, J. R., Kostov, Y., Hausmann, U., Ferreira, D., et al. (2014b). The ocean's role in polar climate change: Asymmetric Arctic and Antarctic responses to greenhouse gas and ozone forcing. *Philosophical Transactions of the Royal Society A*, *372*, 20130040. https://doi.org/10.1098/rsta.2013.0040

Marshall, J., Donohoe, A., Ferreira, D., & McGee, D. (2014a). The ocean's role in setting the mean position of the inter-tropical convergence zone. *Climate Dynamics*, *42*(7–8), 1967–1979. https://doi.org/10.1007/s00382-013-1767-z

McCarthy, G. D., Brown, P. J., Flagg, C. N., Goni, G., Houpert, L., Hughes, C. W., et al. (2020). Sustainable observations of the AMOC: Methodology and technology. *Reviews of Geophysics*, *58*(1), e2019RG000654. https://doi.org/10.1029/2019RG000654

McCarthy, G. D., Smeed, D. A., Johns, W. E., Frajka-Williams, E., Moat, B. I., Rayner, D., et al. (2015). Measuring the Atlantic meridional overturning circulation at 26°N. *Progress in Oceanography*, *130*, 91–111. https://doi.org/10.1016/j.pocean.2014.10.006

Meehl, G. A., Goddard, L., Boer, G., Burgman, R., Branstator, G., Cassou, C., et al. (2013). Decadal climate prediction: An update from the trenches. *Bulletin of the American Meteorological Society*, *95*, 243–267. https://doi.org/10.1175/BAMS-D-12-00241.1

Meinen, C. S., Baringer, M. O., & Garcia, R. F. (2010). Florida current transport variability: An analysis of annual and longer-period signals. *Deep Sea Research Part I: Oceanographic Research Papers*, *57*, 835–846. https://doi.org/10.1016/j.dsr.2010.04.001

Meinen, C. S., Speich, S., Perez, R. C., Dong, S., Piola, A. R., Garzoli, S. L., et al. (2013). Temporal variability of the meridional overturning circulation at 34.5°S: Results from two pilot boundary arrays in the South Atlantic. *Journal of Geophysical Research: Oceans*, *118*, 6461–6478. https://doi.org/10.1002/2013jc009228

Meinen, C. S., Speich, S., Piola, A. R., Ansorge, I., Campos, E., Kersalé, M., et al. (2018). Meridional overturning circulation transport variability at 34.5°S during 2009-2017: Baroclinic and barotropic flows and the dueling influence of the boundaries. *Geophysical Research Letters*, *45*, 4180–4188. https://doi.org/10.1029/2018GL077408

Mercier, H., Lherminier, P., Sarafanov, A., Gaillard, F., Daniault, N., Desbruyères, D., et al. (2015). Variability of the meridional overturning circulation at the Greenland-Portugal OVIDE section from 1993 to 2010. *Progress in Oceanography*, *132*, 250–261. https://doi.org/10.1016/j.pocean.2013.11.001

Peterson, R. G., & Stramma, L. (1991). Upper-level circulation in the South Atlantic Ocean. *Progress in Oceanography*, *26*, 1–73. https://doi.org/10.1016/0079-6611(91)90006-8

Pujol, M.-I., Faugère, Y., Taburet, G., Dupuy, S., Pelloquin, C., Ablain, M., & Picot, N. (2016). DUACS DT2014: The new multi-mission altimeter data set reprocessed over 20 years. *Ocean Science*, *12*(5), 1067–1090. https://doi.org/10.5194/os-12-1067-2016

Rahmstorf, S., Box, J. E., Feulner, G., Mann, M. E., Robinson, A., Rutherford, S., & Schaffernicht, E. J. (2015). Exceptional twentieth-century slowdown in Atlantic Ocean overturning circulation. *Nature Climate Change*, *5*, 475–480. https://doi.org/10.1038/nclimate2554

Richardson, P. L. (2007). Agulhas leakage into the Atlantic estimated with subsurface floats and surface drifters. *Deep Sea Research Part I: Oceanographic Research Papers*, *54*, 1361–1389. https://doi.org/10.1016/j.dsr.2007.04.010

Soutelino, R. G., da Silveira, I. C. A., Gangopadhyay, A., & Miranda, J. A. (2011). Is the Brazil current eddy-dominated to the north of 20°S?. *Geophysical Research Letters*, *38*, L03607. https://doi.org/10.1029/2010GL046276

Srokosz, M. A., & Bryden, H. L. (2015). Observing the Atlantic meridional overturning circulation yields a decade of inevitable surprises. *Science*, *348*, 1255575. https://doi.org/10.1126/science.1255575

Stouffer, R. J., Yin, J., Gregory, J. M., Dixon, K. W., Spelman, M. J., Hurlin, W., et al. (2006). Investigating the causes of the response of the thermohaline circulation to past and future climate changes. *Journal of Climate*, *19*(8), 1365–1387. https://doi.org/10.1175/JCLI3689.1

Sun, C., Thresher, A., Keeley, R., Hall, N., Hamilton, M., Chinn, P. et al. (2010). The data management system for the global temperature and salinity profile programme. In J. Hall, D. E. Harrison, & D. Stammer (Eds.), Proceedings of OceanObs.09: Sustained Ocean Observations and Information for Society (Vol. 2). Venice: ESA Publ.WPP-306. https://doi.org/10.5270/OceanObs09.cwp.86

Trenberth, K. E., Zhang, Y., Fasullo, J. T., & Cheng, L. (2019). Observation-based estimates of global and basin ocean meridional heat transport time series. *Journal of Climate*, *32*(14), 4567–4583. https://doi.org/10.1175/jcli-d-18-0872.1

Vélez-Belchí, P., Pérez-Hernández, M. D., Casanova-Masjoan, M., Cana, L., & Hernández-Guerra, A. (2017). On the seasonal variability of the Canary Current and the Atlantic meridional overturning circulation. *Journal of Geophysical Research: Oceans*, *122*, 4518–4538. https://doi.org/10.1002/2017JC012774

Vellinga, M., & Wood, R. A. (2002). Global climatic impacts of a collapse of the Atlantic thermohaline circulation. *Climatic Change*, *54*(3), 251–267. https://doi.org/10.1023/A:1016168827653

Volkov, D. L., Lee, S. K., Domingues, R., Zhang, H., & Goes, M. (2019). Interannual sea level variability along the southeastern seaboard of the United States in relation to the gyre-scale heat divergence in the North Atlantic. *Geophysical Research Letters*, *46*(13), 7481–7490. https://doi.org/10.1029/2019GL083596

Willis, J. K. (2010). Can in situ floats and satellite altimeters detect long-term changes in Atlantic ocean overturning?. *Geophysical Research Letters*, *37*, L06602. https://doi.org/10.1029/2010GL042372

Zhang, R. (2008). Coherent surface-subsurface fingerprint of the Atlantic meridional overturning circulation. *Geophysical Research Letters*, *35*, L20705. https://doi.org/10.1029/2008GL035463

Zhang, R., & Delworth, T. L. (2005). Simulated tropical response to a substantial weakening of the Atlantic thermohaline circulation. *Journal of Climate*, *18*(12), 1853–1860. https://doi.org/10.1175/JCLI3460.1

Zhao, J., & Johns, W. (2014). Wind-forced interannual variability of the Atlantic meridional overturning circulation at 26.5°N. *Journal Geophysical Research: Oceans*, *119*, 2403–2419. https://doi.org/10.1002/2013JC009407